Theoretical and experimental study on a mechatronic speed variator device for HD Fuel-Injection-Common Rail Pump

(Article begins on next page)

15 May 2024

Department of Electrical and Information Engineering

Electrical and Information Engineering Ph.D. Program

SSD: ING-INF/04–AUTOMATICA

Final Dissertation

Theoretical and experimental study on a mechatronic speed variator device for HD Fuel-Injection-Common Rail Pump

by

Michele Tomaselli

Supervisors:

Prof. Paolo Lino

Prof. Giuseppe Carbone

Coordinator of Ph.D Program:
Prof. Luigi Alfredo Grieco

Course n°33, 01/11/2017-31/10/2020

Politecnico di Bari

LIBERATORIA PER L'ARCHIVIAZIONE DELLA TESI DI DOTTORATO

Al Magnifico Rettore
del Politecnico di Bari

Il/la sottoscritto __Michele Tomaselli__ nato a __Acquaviva delle fonti__ il __01/09/1990__

residente a __Cassano delle Murge__ in via __Alcide de Gasperi, 54__ e-mail __michele_tomaselli@live.it__

iscritto al 3° anno di Corso di Dottorato di Ricerca in __Ingegneria elettrica e dell'Informazione__ ciclo __33__

ed essendo stato ammesso a sostenere l'esame finale con la prevista discussione della tesi dal titolo:

__Theoretical and experimental study on a mechatronic speed variator device for HD Fuel-Injection-Common Rail Pump__

DICHIARA

1) di essere consapevole che, ai sensi del D.P.R. n. 445 del 28.12.2000, le dichiarazioni mendaci, la falsità negli atti e l'uso di atti falsi sono puniti ai sensi del codice penale e delle Leggi speciali in materia, e che nel caso ricorressero dette ipotesi, decade fin dall'inizio e senza necessità di nessuna formalità dai benefici conseguenti al provvedimento emanato sulla base di tali dichiarazioni;
2) di essere iscritto al Corso di Dottorato di ricerca __Ingegneria elettrica e dell'Informazione__ ciclo __33__, corso attivato ai sensi del *"Regolamento dei Corsi di Dottorato di ricerca del Politecnico di Bari"*, emanato con D.R. n.286 del 01.07.2013;
3) di essere pienamente a conoscenza delle disposizioni contenute nel predetto Regolamento in merito alla procedura di deposito, pubblicazione e autoarchiviazione della tesi di dottorato nell'Archivio Istituzionale ad accesso aperto alla letteratura scientifica;
4) di essere consapevole che attraverso l'autoarchiviazione delle tesi nell'Archivio Istituzionale ad accesso aperto alla letteratura scientifica del Politecnico di Bari (IRIS-POLIBA), l'Ateneo archivierà e renderà consultabile in rete (nel rispetto della Policy di Ateneo di cui al D.R. 642 del 13.11.2015) il testo completo della tesi di dottorato, fatta salva la possibilità di sottoscrizione di apposite licenze per le relative condizioni di utilizzo (di cui al sito http://www.creativecommons.it/Licenze), e fatte salve, altresì, le eventuali esigenze di "embargo", legate a strette considerazioni sulla tutelabilità e sfruttamento industriale/commerciale dei contenuti della tesi, da rappresentarsi mediante compilazione e sottoscrizione del modulo in calce (Richiesta di embargo);
5) che la tesi da depositare in IRIS-POLIBA, in formato digitale (PDF/A) sarà del tutto identica a quelle **consegnate**/inviate/da inviarsi ai componenti della commissione per l'esame finale e a qualsiasi altra copia depositata presso gli Uffici del Politecnico di Bari in forma cartacea o digitale, ovvero a quella da discutere in sede di esame finale, a quella da depositare, a cura dell'Ateneo, presso le Biblioteche Nazionali Centrali di Roma e Firenze e presso tutti gli Uffici competenti per legge al momento del deposito stesso, e che di conseguenza va esclusa qualsiasi responsabilità del Politecnico di Bari per quanto riguarda eventuali errori, imprecisioni o omissioni nei contenuti della tesi;
6) che il contenuto e l'organizzazione della tesi è opera originale realizzata dal sottoscritto e non compromette in alcun modo i diritti di terzi, ivi compresi quelli relativi alla sicurezza dei dati personali; che pertanto il Politecnico di Bari ed i suoi funzionari sono in ogni caso esenti da responsabilità di qualsivoglia natura: civile, amministrativa e penale e saranno dal sottoscritto tenuti indenni da qualsiasi richiesta o rivendicazione da parte di terzi;
7) che il contenuto della tesi non infrange in alcun modo il diritto d'Autore né gli obblighi connessi alla salvaguardia di diritti morali od economici di altri autori o di altri aventi diritto, sia per testi, immagini, foto, tabelle, o altre parti di cui la tesi è composta.

Luogo e data __Cassano delle Murge, 16/03/2021__   Firma _____

Il/La sottoscritto, con l'autoarchiviazione della propria tesi di dottorato nell'Archivio Istituzionale ad accesso aperto del Politecnico di Bari (POLIBA-IRIS), pur mantenendo su di essa tutti i diritti d'autore, morali ed economici, ai sensi della normativa vigente (Legge 633/1941 e ss.mm.ii.),

CONCEDE

- al Politecnico di Bari il permesso di trasferire l'opera su qualsiasi supporto e di convertirla in qualsiasi formato al fine di una corretta conservazione nel tempo. Il Politecnico di Bari garantisce che non verrà effettuata alcuna modifica al contenuto e alla struttura dell'opera.
- al Politecnico di Bari la possibilità di riprodurre l'opera in più di una copia per fini di sicurezza, back-up e conservazione.

Luogo e data __Cassano delle Murge, 16/03/2021__   Firma _____

Department of Electrical and Information Engineering

Electrical and Information Engineering Ph.D. Program

SSD: ING-INF/04–AUTOMATICA

Final Dissertation

Theoretical and experimental study on a mechatronic speed variator device for HD Fuel-Injection-Common Rail Pump

by
Michele Tomaselli

Referees:

Prof. Alessandro Rizzo

Prof. Milan Rapaić

Supervisors:

Prof. Paolo Lino

Prof. Giuseppe Carbone

Coordinator of Ph.D Program:
Prof. Luigi Alfredo Grieco

Course n°33, 01/11/2017-31/10/2020

Contents

List of Figures

List of Tables

Abstract

From a historical point of view, the diffusion and the great success of diesel engines were induced by the introduction of the Common-Rail System (CRS). This injection system enabled precise metering of the fuel through the injector nozzles by acting on injection timings and by regulating the common-rail pressure. Moreover, the ability to control the injection pressure made it possible to perform multiple injections, which is the crucial point for the modern diesel engine to reduce pollutant emissions. The evolution of the CRS over time is mostly related to the method used to control the rail pressure. Initially, the common-rail pressure regulation was performed by the so-called Pressure control valve (PCV). This valve was mounted directly on the common-rail or, equivalently, on the outlet port of the pump. This topology ensures a fast and precise regulation of the pressure by discharging the fuel in excess to the tank. The main drawback of this approach is represented by the pressure fluctuations due to the valve functioning, which acts as disturbances on the operation of the injectors. Furthermore, the recirculation of the compressed flow to the tank causes energy dissipation and undesired heating in the fuel tank. To overcome the disadvantages of the PCV, in the modern CRS was introduced a Fuel Metering Unit (FMU), which consists of a valve mounted on the high-pressure pump to adjusts its inlet flow and thus control the common-rail pressure. This kind of regulation reduces energy dissipation because the quantity of fuel compressed by the pump and delivered to the rail is exactly the quantity set by the ECU to obtain the proper air/fuel ratio.

The new topology of CRS proposed in this work, which is still under development, introduces a Continuously Variable Transmission (CVT) between the engine and the high-pressure pump in place of a conventional gear coupling. It enables the adjustment of the pump speed according to the required common-rail pressure and demanded injection flow, thus reducing mechanical losses in the high-pressure pump.

In this work, we summarize the main results obtained investigating the effectiveness of this novel approach. In particular, we present the control strategy for a complete CRS equipped with a continuously variable transmission, which has been validated in simulation, and a preliminary experimental proof of concept performed on a simplified prototype version of the system.

CHAPTER 1

Introduction

1.1 Motivation

Despite the demonization of Diesel engines in the last years, this technology will continue to play a fundamental role in the next years. It is well known that this kind of engine has a big market that is not only related to passenger cars. Indeed, Diesel engines are used in marine application, off road vehicles and heavy duty transportation. As the passenger car, also the manufacturer for these applications are slowly pointing their focus to the electrification, but this transformation will require a lot of effort and time and will be satisfactory when the electricity will be generated with clean power plant [1]. In the meanwhile the diesel engine will continue to give a big contribution. For this reason it makes sense to invest effort in this technology, in order to improve the quality of this engines also in the next years.

1.2 Objective

In modern Common-Rail System (CRS), high-pressure pumps are driven by the internal combustion engine in order to deliver a certain amount of fuel into the rail. The flow demand and the rail pressure are defined by the Engine Control Unit (ECU) in order to optimize the injection quality. See Chapter 2 for a detailed description of the Common-rail System.

Currently the high-pressure pump are linked to the internal combustion engine by using spur gears with a fixed ratio. In order to satisfy the flow demand in all operating

points, this value is usually maximized in the design phase in order cover the so called *quantity balance* of the engine. As result, in almost all their life, the high pressure pumps work with an higher speed than what it is actually necessary.

The novel idea described in this thesis is to introduce a Continuously Variable Transmission (CVT) between the internal combustion engine and the high pressure pump. With this new component it is possible to regulate the high pressure pump speed as a function of the optimal injected quantity defined by the Engine Control Unit (ECU). This new topology has to achieve the following goals:

1. Uniform the design of the high pressure pump between all the customers, bu accomplishing their particular requirements;

2. Reduce the high pressure pump speed, with a reduction of the mechanical power losses and the backflow into the tank as well;

3. Optimize the production and test design of the high pressure pump because the over-speed operating points are no longer used.

This new topology introduces also some non-trivial problems which are the core of the research activities and will be discussed in this thesis. The first problem is related to the study of the CVT it self. Of course this new component must be compact, efficient and reliable. Market and literature offer a number of possible devices that can satisfy this requirements. In this work a traction drive CVT has been chosen. In particular a two-planetary traction drive device known as *NuVinci*. In Chapter 3 is described this device and is developed the mathematical model to compute the efficiency of the transmission. Once the transmission is defined and characterized, it is necessary to define a control strategy for the high pressure fuel regulation. In the new topology there is an actuators redundancy, because the CVT introduce a new degree of freedom in definition of the high pressure flow demand. Therefore, a control strategy for a Multiple Input Single Output (MISO) system is necessary. As shown in Chapter 4, this problem is handled using to control loops that are decoupled each other.

Common rail system

To analyse the numerical models and the control strategies of this system, a knowledge of the main components is necessary. In this chapter, we provide an overview of the common-rail system and a description of its main components.

According to engine power demand and rotating speed, (ECU) defines the optimal pressure value of the fuel in the rail. This value can be reached by using solenoid valves. In the early common rail system, the rail pressure was regulated by using the so called *Pressure control valve* (PCV). This valve is mounted directly on the rail or on the outlet port of the pump. It allows a fast and precise regulation of the rail pressure discharging the unnecessary fuel to the tank. On the other hand, the pressure fluctuations due to the valve can act as disturbances on the injectors. Furthermore, the recirculation of the compressed flow to the tank causes energy dissipation and undesired heating in fuel tank.

To manage the problem related to energy dissipation of the PCV, modern common rail system uses the Fuel Metering Unit (FMU). This valve is mounted on the suction side of the high-pressure pump. It controls the common-rail pressure by regulating the pump inlet flow. This valve reduces energy dissipation because the quantity of fuel compressed by the pump and delivered to the rail is strictly the amount required by the ECU. On the other hand, the rail pressure control must consider the time delay that acts on the actuation variable and the cavitation phenomena that may occur in cylinder chamber.

As both strategies present advantages, modern common rail systems are often equipped with both FMU and PCV (CPC - Coupled Pressure Control). This allow a precise

regulation without energy dissipation and the ability to heat the fuel when the engine is cold without the need of fuel heater. This latter strategy can be an interesting method for future common rail systems and as show in the next section is not covered in literature.

1 Fuel Tank
2 High Pressure Pump
3 Fuel Metering Unit
4 Pre-supply pump
5 Fuel Filter
6 Pressure sensor
7 Common rail
8 Pressure Relief valve
9 Injector
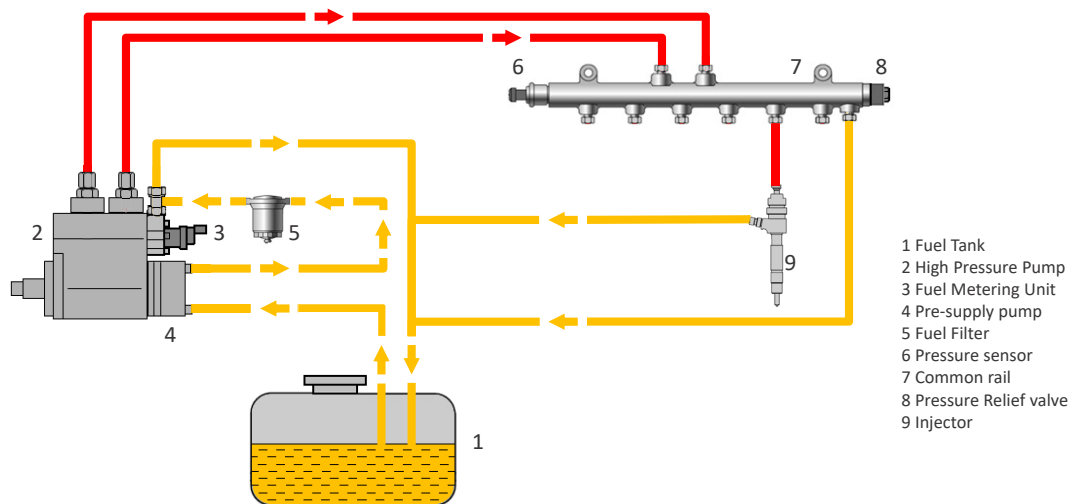
Figure 2.1: Example of a Common Rail system

2.1 Description

Usually, Common rail system can be divided in two main hydraulic circuits: low pressure circuit and high-pressure circuit. The scheme in Fig. 2.1 shows the main components of a common-rail system equipped with a FMU solenoid valve for rail pressure regulation. On rail side is mounted a safety valve (labelled as *Pressure relief valve*). Differently from FMU and PCV, ECU doesn't control this valve, but it opens when the pressure reaches a predefined safety threshold. In the figure is highlighted the division between high pressure components (red lines) and low-pressure components (yellow lines). In particular, low pressure circuit provides fuel from tank to high pressure pump using a pre-supply pump at about 10 bar as maximum pressure. High pressure circuit provides fuel from high pressure pump to rail using a piston pump (2700 bar as maximum). The rail acts as a fuel accumulator. Here, the fuel is pressurized and is ready to the injection phase.

2.1.1   Low pressure pump

In heavy commercial vehicles, an external gear pump is used as low-pressure pump (or pre-supply pump). This pump is mounted on the suction side of the high-pressure pump and is composed by a couple of spur gear driven by the pump camshaft. As shown in Fig. 2.2 the fluid is trapped in the inter-teeth volume and transported into the delivery volume according to the rotating direction of the gears. The meshing of the teeth prevents the backflow from the high-pressure side to the suction side. Obviously, a little amount of leakage is due to backlash and clearance effects [2]. Light vehicles and passenger cars often use electric feed pump mounted in the fuel tank. These pumps are driven by a DC motor, for this reason are able to feed the high-pressure pump with an amount of fuel independent from the engine operating point.
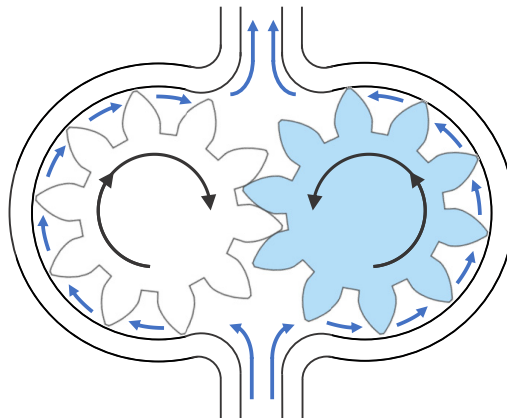
Figure 2.2: Example of an external gear pump

2.1.2   High pressure pump

Reciprocating piston pumps are used as high-pressure pump. These pumps can be "axial" or "radial" according to the position of the pistons in relation to the camshaft. The profile of the cam causes a reciprocating motion of the plunger of the cylinders. In intake phase, the increase of the cylinder volume causes the opening of the suction valve. During compression, the fuel pressure increases due to the decrease of the volume of the cylinder volume. When the pressure inside the cylinder exceeds a

threshold due to the sum of spring preload and its stiffness, the high-pressure valve opens and delivers fuel to the rail.

2.1.3   Solenoid valves

Solenoid valves are electro hydraulic actuator in which a magnetic force is used to move a plunger that regulates the flow through an orifice. When a current is applied to the coil, the magnetic field interacts with the armature of the valve and moves the plunger according to the direction of the magnetic force. If the valve is normally open, the movement of the piston causes the closure of the valve. When no current flow in the coil, the spring pushes the piston into the idle position. PWM modulation is used to change the amplitude of the current in the coil, thus the orifice can be partially opened.

This kind of valves allow pressure regulation in common rail. Valves that are mounted directly on the inlet port of the high-pressure pump act as fuel metering unit (FMU). These valves allow the ECU to regulate the delivery flow of the pump by varying the inlet flow in pump cylinder. PCV valves are mounted on the rail. These valves allow the ECU to regulate the rail pressure by discharging the unnecessary amount of fuel from the rail.

2.1.4   Electro-Injectors

An accurate flow injection is necessary to optimize fuel combustion, to avoid pollutant and to obtain an optimal behaviour of the engine in terms of efficiency. Fuel flow from common-rail fills the accumulation volume and the control chamber. When the solenoid valve is energized, the high-pressure fuel in control chamber flows out through the A-Hole. The subsequent pressure difference between control chamber and the accumulation volume causes the lift of the plunger and the injection of the fuel stored in the accumulation volume through the nozzle.

2.2 State of the art in Common-rail pressure control

Rail pressure regulation represents a non-trivial control problem, due to the complexity of the system, the non-linearity that characterize the components, and the presence of time delays. By assuming the rail as a constant control volume, the pressure dynamic equation can be written as:

$$\frac{dp_r(t)}{dt} = \frac{\beta(p_r(t), T)}{V_r} \left(Q_{in}(t) - Q_{Inj}(t) - Q_{leak}(t) - Q_{PCV}(t) \right) \tag{2.1}$$

where $Q_{in}(t)$ is the flow from high pressure pump, $Q_{inj}(t)$ is the fuel through injectors, $Q_{leak}(t)$ is the leakage flow and $Q_{PCV}(t)$ is the fuel through PCV valve. In eq. (2.1) one can observe that the only quantities that allow a regulation of the pressure dynamic are the fuel flow from the pump and the discharging flow through the PCV. In recent years, many researchers have focused their attention on the definition of advanced control laws for the common rail pressure regulation. Due to the complexity of the system, the non-linearities that characterize the components and the presence of time delays between fuel metering valve actuation and rail pressure variation, this regulation represent a non-trivial control problem.

[3] developed hybrid models of the high pressure pump and injectors. Such models contain a state flow in which each state describes a working phase of the component. Considering the high-pressure pump, the states represent the intake phase and the compression phase respectively, while the state transitions are defined by the pump camshaft operations. Similarly, the injector models are synchronized with the engine crankshaft and describe the three injection phases. The fuel metering valve model contains the RL circuit of the solenoid and the current-flow characteristic curve. Pressure regulation is achieved using a cascade control with two control loops. The outer loop is synchronized with intake phases of the pump cylinders. This control is "event-based" and provide the amount of fuel flow $Q_{HP}(t)$ necessary to take the rail pressure error to zero. More in details, this is achieved by using a PI controller with anti-windup and feed-forward action. The inner loop uses the information provided by the outer loop

and defines the PWM duty cycle that drives the FMU solenoid. Due to the different sample time of the signals involved in the control loops, authors provide a proper sample time conversion method to avoid numerical instability. The control performances have been compared with a standard controller designed using a mean-value model of the system. The comparison shows that the proposed method allows better tracking performances and the simplification of the control structure. In [4], the same authors propose an approach to estimate the FMU current, and compare simulation and experimental results. In both these works the proposed control strategies are tested using the hybrid models used to design the controllers, without taking into consideration uncertainties.

In [5], and in [6],it has been proposed a detailed state space model of a common rail system with a PCV solenoid valve. The model is validated comparing its output to the experimental rail pressure, for different camshaft speeds and PCV duty cycle profiles. The model output is also compared with the data generated by a highly detailed AMESim model. The proposed model is then simplified by adopting some proper assumptions, obtaining a second order state space model suitable for control design. The resulting model is used to develop a sliding mode control law to regulate the rail pressure. To improve control performances, authors includes a model based feed-forward action able to compensate the pressure fluctuation caused by the injection process. The control approach performances are evaluated in different working conditions, in terms of load and speeds.

[7] and [8] developed a discrete time controller using the linear fractional transform (LFT) approach to design a H_∞ controller. The common rail systems considered in these works include both the PCV and the FMU valves, however the control strategy only exploits the latter one. The first step in controller design is the linearization of the model described in [9]. The resulting linear parameter varying model (LPV) is used by the authors to derive a controller in LFT representation using the H_∞ theory. The effectiveness of the proposed control scheme is evaluated on a real vehicle in [10], by implementing the control law on a fixed point 16 bit microcontroller. The obtained results are then compared with a gain scheduled PID showing better tracking

performances and robustness against parameters variation. A deeper analysis of the methodology is made in [11].

[12] proposed a QFT-based controller using the FMU valve. The controller design starts from the definition of a nominal plant, which is obtained by an identification process in the frequency domain. To take into account model uncertainties, the authors added a random perturbation to each parameter of the identified plant. The resulting plants (one for each set of parameters) are studied in the frequency domain by means of the Nichols chart. In particular, for a each frequency on the Nichols chart, there is a group of point (one for each plant). These groups of points are called *plant templates*. Finally, the authors design the controller by imposing the frequency domain specification to the plant templates. At the end of this process, the authors define a discrete time transfer function satisfying the frequency domain specifications. To validate the control strategy, an experimental test is performed on a real common rail system showing good tracking performances.

[13], [14], developed a coupled control strategy using both FMU and PCV. The authors provide a separate controls for each valve, and present an empirical model relating the PCV current to the rail pressure. More in details, it consists in a polynomial equation in which the coefficients are related to the camshaft speed. The model is validated by means of experimental tests performed at constant speed and varying PCV current. The experimental data is compared with the model using the square correlation coefficient R^2. By inverting the model polynomial equation, the authors define a feed-forward term for a PI controller with anti-windup. Similarly, the FMU loop includes in a PI with anti-windup and feed-forward term, which obtained considering the fuel amount requested for the current working conditions. The controllers are validated on a test bench with a 2.2l four-cylinder Diesel engine equipped with a VGT and an EGR. The tests are performed considering the *New European Driving Cycle - (NEDC)* and show good tracking performances. A QFT controller for the PCV control loop [15], where the FMU controller is the same of the previous work. The results show better tracking performances then the others standard PID controllers and a reduced settling time.

[16] proposed two control strategies starting from a non-linear 0D model of the common rail system. The model is mainly represented by the eq. (2.1), in which every flow term is expressed by a look-up-table. The model includes the high-pressure pump delivery flow, the injected flow, and the leakage flow through the injectors. The look-up-tables are expressed as functions of the engine speed, the rail pressure, the FMU current, and the injection timings. To design the controllers, it is performed an input to state linearization of the model. The input variable of this linearized model is the sum of the FMU current and of a term compensating the system non-linearities (obtained from the lookup tables of the non-linear model). Finally, the authors propose two different control strategies: an LQR control with feedforward and integral action, and a LQR controller with integral action. The controllers are tested on the non-linear model and compared with a standard PI controller. The results show best tracking performances and a smoother response. If compared to standard regulators, a further advantage of the proposed approach is that it does not require a specific calibration for each working point.

[17] developed a model-free control for the common rail pressure regulation. To design the controller, the authors introduce the concepts of *ultra-local model* and *intelligent - PI*. The authors define an ultra-local model of the system in the means the model estimation is valid for a very short time for each iteration. The resulting ultra-local model is used to compensate the system non-linearities, and the regulation is obtained using a PI controller with a feedforward term. The resulting actuation signal is directly related to the desired error dynamics and to the estimation error. Simulation results, obtained both in MATLAB/Simulink and AMESim environments, show a better trajectory tracking, with respect to a PID controller and an Active Disturbance Rejection controller.

Traction drive CVT

3.1 Introduction

The dedication to green technology and the environmental care from society and governments increase exponentially in the recent years. Car manufacturers have to face with rules and technology constraints that became more and more strictly. For these reasons, researchers and engineers have focused their works on the improvements in terms of emissions and fuel reduction in internal combustion engines. One of the most promising solution to improve these performances is the adoption of a Continuously Variable Transmission (CVT). These transmissions are able to vary their speed ratios in a continuous and smooth way. Such characteristic is useful to reduce fuel consumption in traditional internal combustion engine. [18] analyse the impact of the adoption of different CVT architecture in a mid class of passenger car. Furthermore, a variable transmission can be used in hybrid powertrain to manage their complex architecture. [19] show that in a pure electric vehicle, the adoption of a CVT transmission can improve efficiency performances.

In this work, we propose a steady state model of a novel CVT traction drive. In these transmissions, a so called *traction oil* is used to transmit power trough the CVT. Due to the its rheological properties, the viscosity of the traction oil increase under high contact pressure. In these way there is no need of belt, chain or teeth meshing. Without these mechanical constraints, the transmission ratio can be changed by varying the angle between the axes of rotation [20]. Our model provides the efficiency curves of the transmission in terms of speed and torque efficiency. The speed efficiency is affected

by slip between the contact bodies while, the torque efficiency is affected by spin and bearing losses. The steady state model can be generalized for dynamic condition by including the inertia of rotating bodies to evaluate the variation of angular speed and the variation of transmission ratio [21].

3.2   Kinematic analysis of the CVT

3.2.1   Geometrical description
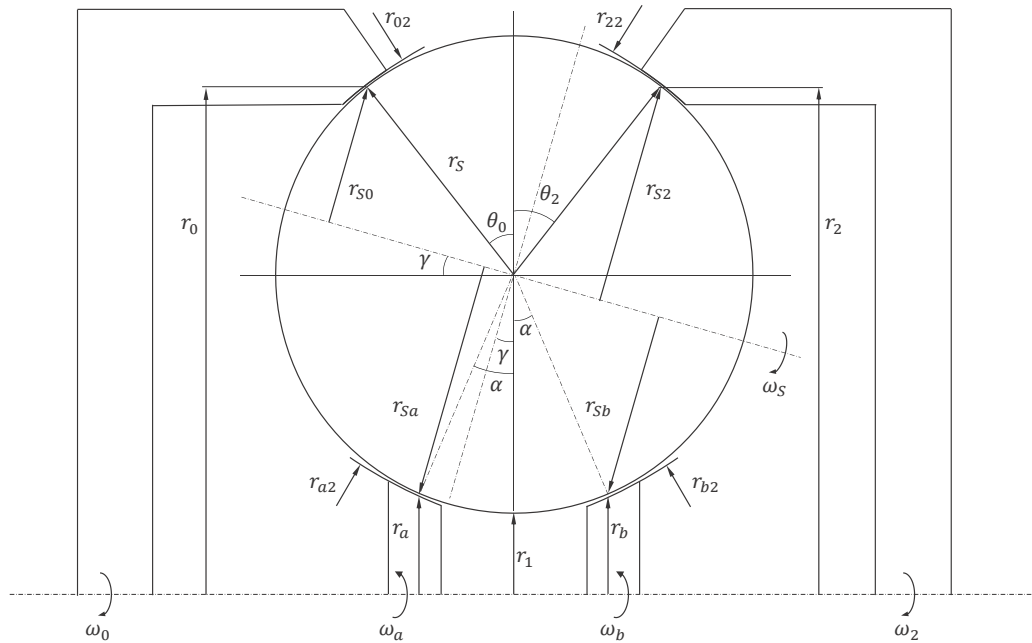
Figure 3.1: CVT Geometrical quantities in the cross sectional view of the transmission

The scheme in Fig. (3.1) shows the main geometrical quantities of the transmission. The half cone angles ϑ_0, α and ϑ_2 are the angles between the horizontal axis and the tangent at the roller passing through the four points of contact, respectively with input disk, sun shafts and output disk. Moreover, γ is the angle between the horizontal axis and the rotation axis of the roller (here in after *Tilt Angle*). The quantities r_a and r_b are the radii of two idle shafts. These shafts are free to move and are used to keep the rollers in contact with the external disks. Finally r_{02}, r_{1a2}, r_{1b2} and r_{22} are the second principal radii of curvature along tangential direction for the points of contact respectively for: input disk, the sun shafts and output disk. Due to its spherical

shape, the principal radii of curvature of the rollers is always equal to r_B. This CVT can be considered as a two stages planetary gear in which the planets dimension can be changed according the desired reduction ratio. According to the geometry of the transmission, following relation hold true:

$$r_{S0} = r_S cos(\vartheta_1 + \gamma) \tag{3.1}$$

$$r_{Sa} = r_S cos(\alpha - \gamma) \tag{3.2}$$

$$r_{Sb} = r_S cos(\alpha + \gamma) \tag{3.3}$$

$$r_{S2} = r_S cos(\vartheta_2 - \gamma) \tag{3.4}$$

Similarly, r_0 and r_2 can be written as:

$$r_0 = r_1 + r_S + r_S cos(\vartheta_0) = r_S[1 + k + cos(\vartheta_0)] \tag{3.5}$$

$$r_a = r_1 + r_S - r_S cos(\alpha) = r_S[1 + k - cos(\alpha)] \tag{3.6}$$

$$r_b = r_1 + r_S - r_S cos(\alpha) = r_S[1 + k - cos(\alpha)] \tag{3.7}$$

$$r_2 = r_1 + r_S + r_S cos(\vartheta_2) = r_S[1 + k + cos(\vartheta_2)] \tag{3.8}$$

where $k = r_1/r_B$ is defined as the *Aspect Ratio*. Here in after these parameters will be express in dimensionless form with respect the roller radius r_B. For example, a generic variable x will be express as $x = \tilde{x} r_B$

3.2.2 Reduction ratio

For each value of γ the CVT can be analysed as a two stage planetary transmission. In ideal conditions, the following relations hold true:

$$\omega_0 r_0 = \omega_S r_{S0}$$
$$\omega_2 r_2 = \omega_S r_{S2} \tag{3.9}$$

Combining equations from (3.1) to (3.9), we are able to define the reduction ratio as a function of the tilt angle γ:

$$\tau_{ID} = \frac{\omega_2}{\omega_0} = \frac{r_{S2}r_0}{r_{S0}r_2} = \frac{cos(\vartheta_2 - \gamma)[1 + k + cos(\vartheta_0)]}{cos(\vartheta_0 + \gamma)[1 + k + cos(\vartheta_2)]} = \tau_0 \frac{cos(\vartheta_2 - \gamma)}{cos(\vartheta_0 + \gamma)} \quad (3.10)$$

If $\vartheta_0 = \vartheta_2 = \vartheta$, the reduction ratio will be:

$$\tau_{ID} = \frac{cos(\vartheta - \gamma)}{cos(\vartheta + \gamma)} \quad (3.11)$$

The evaluation of the reduction ratio range needs the definition of an admissible range for tilt angle. Referring to Fig. 3.1 following conditions hold true:

$$\gamma > max\left(-\vartheta_0, \left[\vartheta_2 - \frac{\pi}{2}\right]\right)$$

$$\gamma < min\left(\vartheta_2, \left[\frac{\pi}{2} - \vartheta_0\right]\right) \quad (3.12)$$

Fig. 3.3 shows the ideal reduction ratios at different values of ϑ. Obviously, constraints shown in (3.12) derive from pure geometrical consideration. In a practical implementation, this range should take into account the tilt angle actuation system and the bearing on the rollers. In our model, this range has been reduced by introducing a safety factor of 0.8.

3.2.3 Creep and spin losses

As we show in the next sections, the transmission of torque is due to the difference of tangential speed in the region of contact between the rotating bodies. For this reason, in real devices a little amount of creep is always present. To evaluate the transmission in presence of creep, we define the creep coefficients C_{R0}, C_{Ra}, C_{Rb} and C_{R2} as follow:

$$C_{R0} = \frac{|\omega_0|r_0 - |\omega_S|r_{S0}}{|\omega_0|r_0} \qquad C_{Ra} = \frac{|\omega_S|r_{Sa} - |\omega_a|r_a}{|\omega_S|r_{Sa}}$$

$$C_{Rb} = \frac{|\omega_S|r_{Sb} - |\omega_b|r_b}{|\omega_S|r_{Sb}} \qquad C_{R2} = \frac{|\omega_S|r_{S2} - |\omega_2|r_2}{|\omega_S|r_{S2}} \quad (3.13)$$
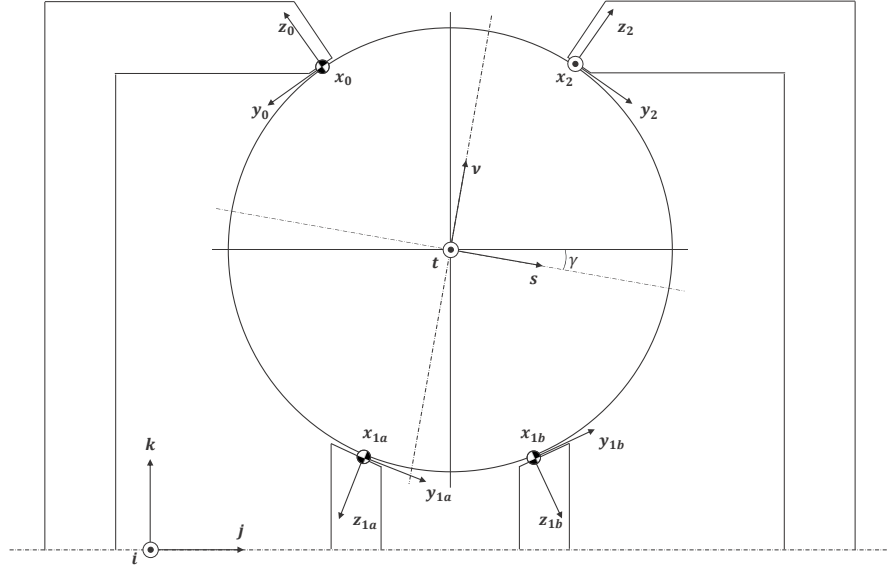
**Figure 3.2:** Reference systems of the rotating bodies

Considering creep coefficients, we can rephrase the reduction ration in eq. 3.10 as:

$$\tau_R = \frac{\omega_2 \omega_S}{\omega_S \omega_0} = \frac{r_0 r_{S2}}{r_{S0} r_2}(1 - C_{R0})(1 - C_{R2}) = \tau_{ID}(1 - C_{R0})(1 - C_{R2}) \tag{3.14}$$

Creep can be thought as a loss in transmission of speed through the CVT. In this way, we are able to define the efficiency of the CVT in terms of speed transmission:

$$\eta_{Speed} = \frac{\tau_R}{\tau_{ID}} = (1 - C_{R0})(1 - C_{R2}) \tag{3.15}$$

 Spin consists of parasitic axis of rotation that acts along normal direction in the point of contact between two rotating bodies. It causes losses in torque transmission and can generate considerable side forces on the rotating bodies [22]. [20] have developed a model of the Half-Toroidal CVT that take in account this effect. As shown in Fig. 3.1 and considering the reference systems defined in 3.2, the angular velocity of each
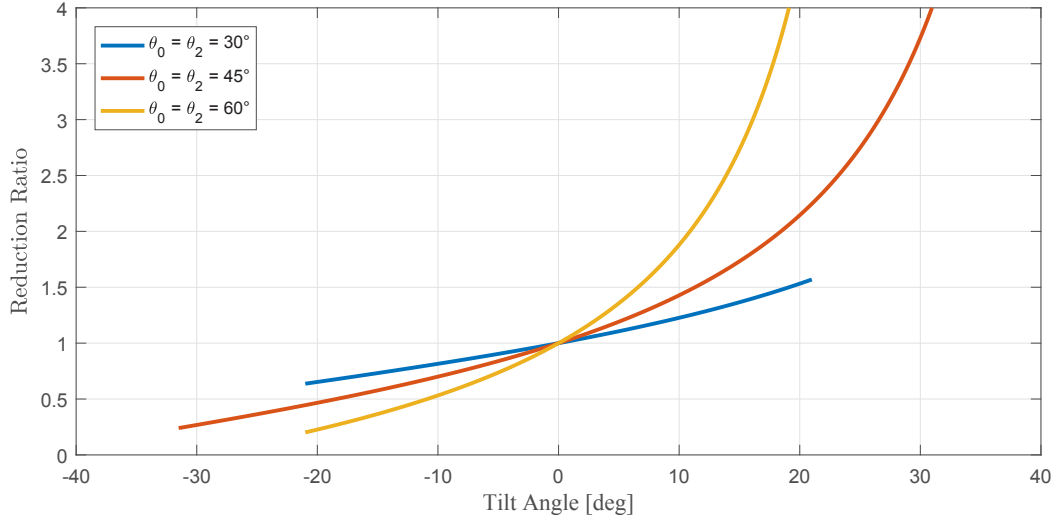
Figure 3.3: Reduction ratio at different values of $\vartheta_0 = \vartheta_2$

rollers relative to the other bodies can be evaluated as follow:

$$
\begin{aligned}
\boldsymbol{\omega_{S0}} &= |\omega_S|\boldsymbol{j} - |\omega_0|\boldsymbol{s} &= |\omega_S|\left[cos(\gamma)\boldsymbol{j} - sin(\gamma)\boldsymbol{k}\right] - |\omega_0|\boldsymbol{j} \\
\\
\boldsymbol{\omega_{Sa}} &= |\omega_S|\boldsymbol{j} + |\omega_a|\boldsymbol{s} &= |\omega_S|\left[cos(\gamma)\boldsymbol{j} - sin(\gamma)\boldsymbol{k}\right] + |\omega_a|\boldsymbol{j} \\
\\
\boldsymbol{\omega_{Sb}} &= |\omega_S|\boldsymbol{j} + |\omega_S|\boldsymbol{s} &= |\omega_S|\left[cos(\gamma)\boldsymbol{j} - sin(\gamma)\boldsymbol{k}\right] + |\omega_b|\boldsymbol{j} \\
\\
\boldsymbol{\omega_{S2}} &= |\omega_S|\boldsymbol{j} - |\omega_2|\boldsymbol{s} &= |\omega_S|\left[cos(\gamma)\boldsymbol{j} - sin(\gamma)\boldsymbol{k}\right] - |\omega_2|\boldsymbol{j}
\end{aligned}
\tag{3.16}
$$

The spin velocity is defined as the normal component of the relative speed acting on the contact point. is the angular velocity of each rollers relative to the output disk. The spin speed are defined as the normal component of the relative speed acting on the point of contact. After some geometrical consideration, we can define the spin
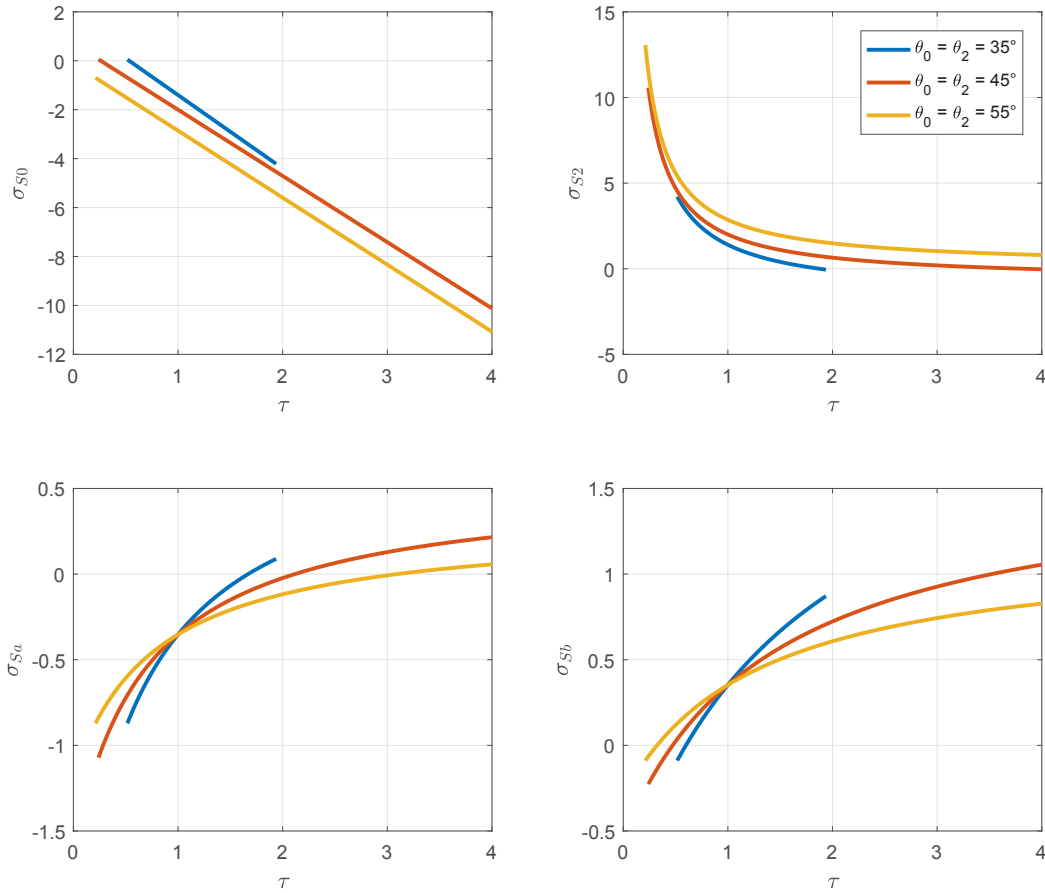
coefficients as follow:

$$\sigma_{S0} = \frac{\boldsymbol{\omega_{S0}} \cdot \boldsymbol{z_0}}{|\omega_0|} = \tilde{r}_0 tan(\vartheta_0 + \gamma)(1 - C_{R0}) - sin(\vartheta_0) \tag{3.17}$$

$$\sigma_{Sa} = \frac{\boldsymbol{\omega_{Sa}} \cdot \boldsymbol{z_a}}{|\omega_a|} = -sin(\alpha) - \frac{\tilde{r}_a tan(\alpha - \gamma)}{(1 - C_{Ra})} \tag{3.18}$$

$$\sigma_{Sb} = \frac{\boldsymbol{\omega_{Sb}} \cdot \boldsymbol{z_b}}{|\omega_b|} = \frac{\tilde{r}_b tan(\alpha + \gamma)}{(1 - C_{Rb})} + sin(\alpha) \tag{3.19}$$

$$\sigma_{S2} = \frac{\boldsymbol{\omega_{S2}} \cdot \boldsymbol{z_2}}{|\omega_2|} = \frac{\tilde{r}_2 tan(\vartheta_2 - \gamma)}{(1 - C_{R2})} - sin(\vartheta_2) \tag{3.20}$$

Figure 3.4: Spin coefficients at different values of half cone angle as a function of reduction ratio

Fig. 3.4 shows the spin coefficients as a function of the tilt angle. To perform these evaluations, we consider an aspect ratio of 1 and the simplifying hypothesis $\vartheta = \vartheta_0 = \vartheta_2$.

Analysing these results, we can observe that there is a relevant amount of spin for each reduction ratio. In fact there is no γ able to nullify spin coefficients in each contact points. Further, considering both Fig. 3.3 and Fig. 3.4, we can notice that the larger is the range of reduction ratio required, the bigger is the amount of spin.

3.3 Forces and Efficiency formulation

The free body diagram in Fig. 3.5 allows us to perform an analysis of the force and torque equilibrium of the system. It is worth noting that the number of the rollers is "n" and we assume that the motor is linked to the disk 0, the load acts on the disk 2
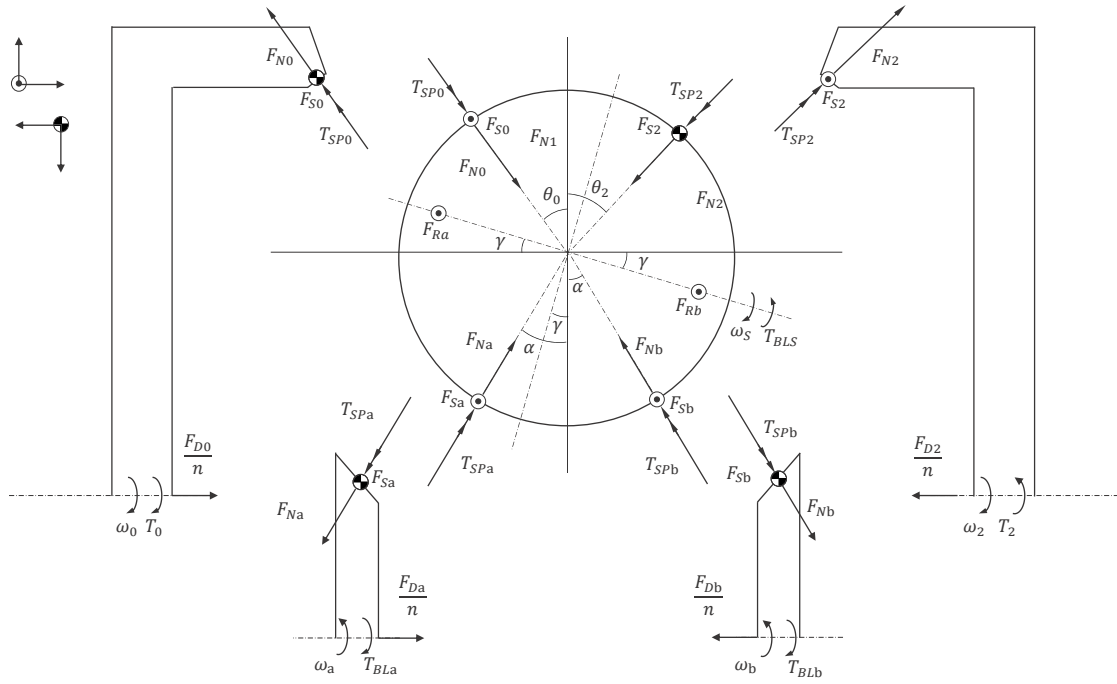
Figure 3.5: Free body diagram of the transmission

and the sun is free to rotate. Tangential forces F_{S0}, F_{Sa}, F_{Sb} and F_{S2} provide torque transmission through the rotating bodies. F_{D0} and F_{D2} are the clamping forces acting on the lateral disks. The normal forces F_{N0}, F_{Na}, F_{Nb} and F_{N2} provide high pressure contact between rollers and disks. The torque analysis must include the input and load torques, respectively T_0 and T_2. As stated before, the spin effect causes torque losses. $T_{SP0}, T_{SPa}, T_{SPb}$ and T_{SP2} are the torques caused by spin phenomena. The bearing friction torques T_{BLS}, T_{BLa} and T_{BLb} act as load on the rollers and on the sun shafts. These friction torques are evaluated using models from literature [23] [24]. These models carry out the friction torque as the sum of two contributions: the load independent friction T_{B0}, and the load dependent friction T_{B1}. In particular, T_{S0} is a

function of the bearing type, the lubrication method and the rotational speed.

$$
T_{B0} = \begin{cases} 160 \cdot 10^{-10} f_0 d^3 & \eta_c N < 2000 \\ \\ 10^{-10} (\eta_c N)^{0.69} f_0 d^3 & \eta_c N > 2000 \end{cases}
\tag{3.21}
$$

where $\eta_c [mm^2/s]$ is the kinematic viscosity of the lubricant, $N[rpm]$ is the rotational speed of the bearing, $d[mm]$ is the bearing mean diameter and $f_0 = 12$ is a coefficient that depends on the bearing type.

While, the load dependent friction torque has been evaluated as follow:

$$
T_{B1} = 10^{-3} f_1 P^a d_m^b
\tag{3.22}
$$

where $a = b = 1$, $f_1 = 3 \cdot 10^{-1}$ is a coefficient that depends on the bearing type and P is the equivalent load. Considering force equilibrium on each rollers, following relations hold true:

$$
F_{S0} + F_{Sa} + F_{Sb} - F_{S2} + F_{Ra} + F_{Rb} = 0
$$

$$
-F_{N0} cos(\vartheta_0) + (F_{Na} + F_{Nb}) cos(\alpha) - F_{N2} cos(\vartheta_2) = 0
\tag{3.23}
$$

$$
F_{N0} sin(\vartheta_0) + F_{Na} sin(\alpha) - F_{Nb} sin(\alpha) - F_{N2} sin(\vartheta_2) = 0
$$

Moreover, considering the torque equilibrium on each roller following relations hold true:

$$
T_{BL} = F_{S0} r_{S0} - F_{Sa} r_{Sa} - F_{Sb} r_{Sb} - F_{S2} r_{S2} +
$$

$$
+ T_{SP0} sin(\vartheta_0 + \gamma) + T_{SPa} sin(\alpha - \gamma) + T_{SPb} sin(\alpha + \gamma) - T_{SP2} sin(\vartheta_2 - \gamma)
\tag{3.24}
$$

$$F_{S0}sin(\vartheta_0 + \gamma)r_B + F_{Sa}sin(\alpha - \gamma)r_B + F_{Sb}sin(\alpha + \gamma)r_B+$$

$$+F_{S2}sin(\vartheta_2 - \gamma)r_B + (F_{Ra} - F_{Rb})0.5r_S - T_{SP0}cos(\vartheta_0 + \gamma)+ \qquad (3.25)$$

$$+T_{spa}cos(\alpha - \gamma) + T_{spb}cos(\alpha + \gamma) - T_{SP2}cos(\vartheta_2 - \gamma) = 0$$

Considering the equilibrium of the input disk, following relations hold true:

$$F_{Din} - nF_{N0}sin(\vartheta_0) = 0 \qquad (3.26)$$

$$T_0 - nF_{S0}r_0 - nT_{SP0}sin(\vartheta_0) = 0 \qquad (3.27)$$

The same analysis on output disk gives the following equations:

$$F_{Dout} - nF_{N2}sin(\vartheta_2) = 0 \qquad (3.28)$$

$$T_2 + nF_{S2}r_2 + nT_{SP2}sin(\vartheta_2) = 0 \qquad (3.29)$$

Considering that the sun shafts are free to rotate, following relations hold true:

$$F_{Da} - nF_{Na}sin(\alpha) = 0 \qquad (3.30)$$

$$T_{BLa} - nF_{Sa}r_a - nT_{SPa}sin(\alpha) = 0 \qquad (3.31)$$

$$F_{Db} - nF_{Nb}sin(\alpha) = 0 \qquad (3.32)$$

$$T_{BLb} - nF_{Sb}r_b + nT_{SPb}sin(\alpha) = 0 \qquad (3.33)$$

$$F_{Da} - F_{Db} = 0 \qquad (3.34)$$

Considering the viscoelastic coupling between the elements, we can define the following traction coefficients:

$$\mu_0 = F_{S0}/F_{N0}$$

$$\mu_a = F_{Sa}/F_{Na}$$

$$\mu_b = F_{Sb}/F_{Nb} \tag{3.35}$$

$$\mu_2 = F_{S2}/F_{N2}$$

Similarly, we can define spin coefficients as follow:

$$\chi_0 = T_{SP0}/(F_{N0}r_0)$$

$$\chi_a = T_{SPa}/(F_{Na}r_a)$$

$$\chi_b = T_{SPb}/(F_{Nb}r_b) \tag{3.36}$$

$$\chi_2 = T_{SP2}/(F_{N2}r_2)$$

Using these coefficients in the simplifying condition $\vartheta = \vartheta_0 = \vartheta_2$, we can rephrase the torques balance of the external disks and of the suns as dimensionless quantities:

$$t_0 = T_0/(nr_0 F_{N0}) = \mu_0 + \sin(\vartheta)\chi_0$$

$$t_{BLa} = T_{BLa}/(nr_a F_{Na}) = \mu_a + \sin(\alpha)\chi_a$$

$$t_{BLb} = T_{BLb}/(nr_b F_{Nb}) = \mu_b - \sin(\alpha)\chi_b \tag{3.37}$$

$$t_2 = T_2/(nr_2 F_{N2}) = -\mu_2 - \sin(\vartheta)\chi_2$$

Moreover, solving of the force balance, we can define contact and clamping forces as a function of the geometrical quantities and F_{n0}:

$$
\begin{cases}
F_{n2} = F_{n0}\frac{sin(\vartheta_0)}{sin(\vartheta_2)} = F_{n0} \\[2ex]
F_{Na} = F_{n0}\frac{sin(\vartheta_0+\vartheta_2)}{2cos(\alpha)sin(\vartheta_2)} = F_{n0}\frac{cos(\vartheta)}{cos(\alpha)} \\[2ex]
F_{Nb} = F_{n0}\frac{sin(\vartheta_0+\vartheta_2)}{2cos(\alpha)sin(\vartheta_2)} = F_{n0}\frac{cos(\vartheta)}{cos(\alpha)} \\[2ex]
F_{D0} = nF_{n0}sin(\vartheta_0) = nF_{n0}sin(\vartheta) \\[2ex]
F_{Da} = nF_{n0}tan(\alpha)\frac{sin(\vartheta_0+\vartheta_2)}{2sin(\vartheta_2)} = nF_{n0}tan(\alpha)cos(\vartheta) \\[2ex]
F_{Db} = nF_{n0}tan(\alpha)\frac{sin(\vartheta_0+\vartheta_2)}{2sin(\vartheta_2)} = nF_{n0}tan(\alpha)cos(\vartheta) \\[2ex]
F_{D2} = nF_{n0}sin(\vartheta_0) = nF_{n0}sin(\vartheta)
\end{cases}
\tag{3.38}
$$

Similarly, using (3.38), we can rephrase the equilibrium equations of the rollers as dimensionless quantities:

$$
t_{BLS} = \frac{T_{BLS}}{F_{N0}r_b} = \tilde{r}_{S0}\mu_0 - \tilde{r}_{Sa}\frac{cos(\vartheta)}{cos(\alpha)}\mu_a - \tilde{r}_{Sb}\frac{cos(\vartheta)}{cos(\alpha)}\mu_b - \tilde{r}_{S2}\mu_2 + \tilde{r}_0 sin(\vartheta+\gamma)\chi_0
$$
$$
+\tilde{r}_a\frac{cos(\vartheta)}{cos(\alpha)}sin(\alpha-\gamma)\chi_a - \tilde{r}_b\frac{cos(\vartheta)}{cos(\alpha)}sin(\alpha+\gamma)\chi_b - \tilde{r}_2 sin(\vartheta-\gamma)\chi_2
\tag{3.39}
$$

$$
sin(\vartheta+\gamma)\mu_0 + \frac{cos(\vartheta)}{cos(\alpha)}sin(\alpha-\gamma)\mu_a - \frac{cos(\vartheta)}{cos(\alpha)}sin(\alpha+\gamma)\mu_b
$$
$$
+sin(\vartheta-\gamma)\mu_2 + 0.5(f_{ra}-f_{rb}) - \tilde{r}_0 cos(\vartheta+\gamma)\chi_0
\tag{3.40}
$$
$$
+\tilde{r}_a\frac{cos(\vartheta)}{cos(\alpha)}cos(\alpha-\gamma)\chi_a + \tilde{r}_b\frac{cos(\vartheta)}{cos(\alpha)}cos(\alpha+\gamma)\chi_b - \tilde{r}_2 cos(\vartheta-\gamma)\chi_2 = 0
$$

$$
\mu_0 + \frac{cos(\vartheta)}{cos(\alpha)}\mu_a + \frac{cos(\vartheta)}{cos(\alpha)}\mu_b - \mu_2 + f_{ra} + f_{rb} = 0
\tag{3.41}
$$

Considering (3.11) and (3.15), we can spread the efficiency in terms of speed and torque components:

$$\eta = \frac{P_2}{P_0} = \frac{T_2\omega_2}{T_0\omega_0} = \frac{T_2\omega_2\tau_{ID}}{T_0\omega_0\tau_{ID}} = \eta_{Speed}\frac{T_2 r_{S2} r_0}{T_0 r_{S0} r_2} = \eta_{Speed}\eta_{Torque} \qquad (3.42)$$

Considering equations (3.11) and (3.37) we can define torque efficiency as a function of tilt angle:

$$\eta_{Torque} = \frac{T_{2R}}{T_{2ID}} = -\tau_{ID}\frac{t_2 n F_{N2} r_2}{t_0 n F_{N0} r_0} = -\tau_{ID}\left[\frac{-\mu_2 - \chi_0 sin(\vartheta)}{\mu_0 + \chi_0 sin(\vartheta)}\right] \qquad (3.43)$$

Finally, global efficiency is:

$$\eta = \eta_{Speed}\eta_{Torque} = \left[\frac{\mu_2 + \chi_2 sin(\vartheta)}{\mu_0 + \chi_0 sin(\vartheta)}\right]\tau_{ID}(1 - C_{R0})(1 - C_{R2}) \qquad (3.44)$$

3.4 Contact model

The development of a contact model that take into account viscoelastic behaviour of traction fluid is a mandatory step to define these coefficients. The model adopted for this purpose is developed according [25] and is based on the evaluation of the pressure distribution over the contact area. Considering the high contact pressure is reasonable to suppose that the pressure distribution is explained by Hertzian theory for dry contact [26]. The film thickness of the traction oil is estimated using the Hamrock-Dowson formula for hard - EHL contact and is supposed to be almost constant in the contact area. The first step to analyse the contact between two surfaces is the evaluation of the equivalent radius of curvature in the point of contact. According to Fig. 3.1, we are able to define the equivalent radii of curvature in dimensionless form as $\tilde{\rho}_{eq} = (r_S/\rho_x + r_S/\rho_y)^{-1}$, where ρ_x is the equivalent radius of curvature in the rolling direction, while ρ_y is the equivalent radius of curvature in the tilting direction.

$$\tilde{\rho}_{eq0x} = \left(\frac{1}{r_{0x}} + \frac{1}{r_{S0x}}\right)^{-1} = \frac{1+k}{r_S\tilde{r}_0}; \qquad \tilde{\rho}_{eq0y} = \left(\frac{1}{r_{0y}} + \frac{1}{r_{S0y}}\right)^{-1} = \frac{\tilde{r}_{02} - 1}{r_{02}} \qquad (3.45)$$

$$\tilde{\rho}_{eqax} = \left(\frac{1}{r_{ax}} + \frac{1}{r_{Sax}}\right)^{-1} = \frac{1+k}{r_S\tilde{r}_a}; \qquad \tilde{\rho}_{eqay} = \left(\frac{1}{r_{ay}} + \frac{1}{r_{Say}}\right)^{-1} = \frac{\tilde{r}_{a2} - 1}{r_{a2}} \qquad (3.46)$$

$$\tilde{\rho}_{eqbx} = \left(\frac{1}{r_{bx}} + \frac{1}{r_{Sbx}}\right)^{-1} = \frac{1+k}{r_S\tilde{r}_b}; \qquad \tilde{\rho}_{eqby} = \left(\frac{1}{r_{by}} + \frac{1}{r_{Sby}}\right)^{-1} = \frac{\tilde{r}_{b2} - 1}{r_{b2}} \qquad (3.47)$$

$$\tilde{\rho}_{eq2x} = \left(\frac{1}{r_{2x}} + \frac{1}{r_{S2x}}\right)^{-1} = \frac{1+k}{r_S\tilde{r}_2}; \qquad \tilde{\rho}_{eq2y} = \left(\frac{1}{r_{2y}} + \frac{1}{r_{S2y}}\right)^{-1} = \frac{\tilde{r}_{22} - 1}{r_{22}} \qquad (3.48)$$

Pressure distribution evaluation needs the calculation of semi axes of contact eclipse $(a_X$ and $a_Y)$. This evaluation is performed using the Hamrock and Brewe method [25]. Eccentricity parameter ϵ and elliptic integral I_1 and I_2 are defined as follow:

$$\epsilon = \frac{\tilde{a}_y}{\tilde{a}_x} = \xi^{2/\pi} \qquad (3.49)$$

$$I_1 = \begin{cases} \frac{\pi}{2} - \left(\frac{\pi}{2} - 1\right) ln(\xi) & \epsilon < 1 \\[2ex] \frac{\pi}{2} + \left(\frac{\pi}{2} - 1\right) ln(\xi) & \epsilon > 1 \end{cases} \qquad (3.50)$$

$$I_2 = \begin{cases} 1 + \left(\frac{\pi}{2} - 1\right) \xi & \epsilon < 1 \\[2ex] 1 + \left(\frac{\pi}{2} - 1\right) \frac{1}{\xi} & \epsilon > 1 \end{cases} \qquad (3.51)$$

Where dimensionless coefficient ξ stands for the ratio between the two principal radii of curvature $\xi = \rho_{eqy}/\rho_{eqx}$. Dimensionless axes a_y and a_x in (3.49) are evaluated respect the contact length parameter Λ defined as follow:

$$\Lambda = \left(\frac{6F_n r_S}{\pi E'}\right)^{\frac{1}{3}} \qquad (3.52)$$

where $E' = E/(1 - \nu^2)$ is the effective elastic modulus, while E and ν are respectively the modulus of elasticity of the contacting bodies and the Poisson's ratio. The contact length parameter is evaluated for each point of contact, to simplify the discussion and

considering that the definition of the following quantities are the same for every point of contact, here in after we avoid the use of the subscript (where unnecessary). Equations (3.45) to (3.52) allow us to evaluate dimensionless semi-axes of contact eclipse for the three points of contact:

$$\tilde{a}_Y = \left(\epsilon^2 I_2 \tilde{\rho}_{eq}\right)^{\frac{1}{3}}; \qquad \tilde{a}_X = \left(I_2 \frac{\tilde{\rho}_{eq}}{\epsilon}\right)^{\frac{1}{3}} \tag{3.53}$$

Using the results of Hertzian theory [25], introducing half-amplitude of the subsurface orthogonal shear stress $\tau_0 = \tau_0 \Lambda^2 / F_n$ and the dimensionless co-ordinates $X = x/a_x$ and $Y = y/a_y$, we are able to define the dimensionless pressure distribution as follow:

$$\tilde{p}_Y = \tilde{p}_{Max}\sqrt{1 - X^2 - Y^2} = \frac{3}{2\pi\tilde{a}_X\tilde{a}_Y}\sqrt{1 - X^2 - Y^2} \tag{3.54}$$

According to the model of contact used in this work, we estimate the fluid viscosity for EHL contact using the relation:

$$\log(\tilde{\eta}) = \log(\eta/\eta_0) = \left[\left(1 + \frac{\pi\tilde{p}}{6\mathfrak{R}\tilde{c}_p}\right)^{z_1} - 1\right]\log(\eta_0/\eta_\infty) \tag{3.55}$$

Where $\tilde{c}_p = c_p/E'$, $c_p = 1.96 \cdot (10)^8$, η is the absolutely viscosity at the pressure p, η_0 is the absolute viscosity at the atmospheric pressure for the given temperature, $\eta_\infty = 6.31 \cdot 10^{-5}$ [Pa s], the dimensionless constant z_1 is the viscosity-pressure index and $\mathfrak{R}$ is the dimensionless load parameter:

$$\mathfrak{R} = \frac{r_S}{\Lambda} = \left(\frac{\pi E' r_S^2}{6F_n}\right)^{1/3} \tag{3.56}$$

Using the procedure presented in [24], we are able to define the shear stress acting on

the roller at the contacts point in rolling and tangential directions:

$$
\begin{aligned}
\tilde{\tau}_{S0x} &= \frac{6}{\pi}\mathfrak{R}_0\tilde{\tau}_{L0}\frac{v_{S0x}}{|\boldsymbol{V_{S0}}|}\left(1-e^{-\frac{\eta_{S0}|\boldsymbol{V_{S0}}|}{h_0\tau_{L0}}}\right); &
\tilde{\tau}_{S0y} &= \frac{6}{\pi}\mathfrak{R}_0\tilde{\tau}_{L0}\frac{v_{S0y}}{|\boldsymbol{V_{S0}}|}\left(1-e^{-\frac{\eta_{S0}|\boldsymbol{V_{S0}}|}{h_0\tau_{L0}}}\right) \\
\tilde{\tau}_{Sax} &= \frac{6}{\pi}\mathfrak{R}_a\tilde{\tau}_{La}\frac{v_{Sax}}{|\boldsymbol{V_{Sa}}|}\left(1-e^{-\frac{\eta_{Sa}|\boldsymbol{V_{Sa}}|}{h_a\tau_{La}}}\right); &
\tilde{\tau}_{Say} &= \frac{6}{\pi}\mathfrak{R}_a\tilde{\tau}_{La}\frac{v_{Say}}{|\boldsymbol{V_{Sa}}|}\left(1-e^{-\frac{\eta_{Sa}|\boldsymbol{V_{Sa}}|}{h_a\tau_{La}}}\right) \\
\tilde{\tau}_{Sbx} &= \frac{6}{\pi}\mathfrak{R}_b\tilde{\tau}_{Lb}\frac{v_{Sbx}}{|\boldsymbol{V_{Sb}}|}\left(1-e^{-\frac{\eta_{Sb}|\boldsymbol{V_{Sb}}|}{h_b\tau_{Lb}}}\right); &
\tilde{\tau}_{Sby} &= \frac{6}{\pi}\mathfrak{R}_b\tilde{\tau}_{Lb}\frac{v_{Sby}}{|\boldsymbol{V_{Sb}}|}\left(1-e^{-\frac{\eta_{Sb}|\boldsymbol{V_{Sb}}|}{h_b\tau_{Lb}}}\right) \\
\tilde{\tau}_{S2x} &= \frac{6}{\pi}\mathfrak{R}_2\tilde{\tau}_{L2}\frac{v_{S2x}}{|\boldsymbol{V_{S2}}|}\left(1-e^{-\frac{\eta_{S2}|\boldsymbol{V_{S2}}|}{h_2\tau_{L2}}}\right); &
\tilde{\tau}_{S2y} &= \frac{6}{\pi}\mathfrak{R}_2\tilde{\tau}_{L2}\frac{v_{S2y}}{|\boldsymbol{V_{S2}}|}\left(1-e^{-\frac{\eta_{S2}|\boldsymbol{V_{S2}}|}{h_2\tau_{L2}}}\right)
\end{aligned}
\tag{3.57}
$$

where h is the film thickness of the oil in the point of contact, while $\tilde{\tau}_L = \tau_L/E'$ and τ_L is the limiting shear stress calculated as:

$$
\tau_L = \tau_{L0} + ap
\tag{3.58}
$$

Dimensionless relative velocities in (3.57) can be evaluated according to the reference frames as shown in Fig. 3.2.

$$
\begin{aligned}
\frac{v_{S0X}}{|\boldsymbol{\omega_0}|r_0} &= C_{R0} - \frac{\sigma_{S0}\tilde{a}_{Y0}Y}{\tilde{r}_0\mathfrak{R}_0}; &
\frac{v_{S0Y}}{|\boldsymbol{\omega_0}|r_0} &= \frac{\sigma_{S0}\tilde{a}_{X0}X}{\tilde{r}_0\mathfrak{R}_0} \\
\frac{v_{SaX}}{|\boldsymbol{\omega_a}|r_a} &= \frac{C_{Ra}}{1-C_{Ra}} - \frac{\sigma_{Sa}\tilde{a}_{Ya}Y}{\tilde{r}_a\mathfrak{R}_a}; &
\frac{v_{SaY}}{|\boldsymbol{\omega_a}|r_a} &= \frac{\sigma_{Sa}\tilde{a}_{Xa}X}{\tilde{r}_a\mathfrak{R}_a} \\
\frac{v_{SbX}}{|\boldsymbol{\omega_b}|r_b} &= \frac{C_{Rb}}{1-C_{Rb}} - \frac{\sigma_{Sb}\tilde{a}_{Yb}Y}{\tilde{r}_b\mathfrak{R}_b}; &
\frac{v_{SbY}}{|\boldsymbol{\omega_b}|r_b} &= \frac{\sigma_{Sb}\tilde{a}_{Xb}X}{\tilde{r}_b\mathfrak{R}_b} \\
\frac{v_{S2X}}{|\boldsymbol{\omega_2}|r_2} &= \frac{C_{R2}}{1-C_{R2}} - \frac{\sigma_{S2}\tilde{a}_{Y2}Y}{\tilde{r}_2\mathfrak{R}_2}; &
\frac{v_{S2Y}}{|\boldsymbol{\omega_2}|r_2} &= \frac{\sigma_{S2}\tilde{a}_{X2}X}{\tilde{r}_2\mathfrak{R}_2}
\end{aligned}
\tag{3.59}
$$

As shown in (3.57) to calculate the shear stress distribution, we need to evaluate the film thickness in the contact region for each point of contact. Using the Hamrock model for elliptical conjunction in EHL contact, we can define the dimensionless central film thickness $H = h/\rho_{eqx}$ in the contact region as follow:

$$H_0 = \Phi\left[(1 - 0.5C_{r0})(1 + k)\tilde{\omega}_0\right]^{0.67} \tilde{\zeta}^{\,0.53} \, \tilde{\rho}_{eq0x}^{\,0.134} \, \mathfrak{R}_0^{\,0.201} \left(1 - 0.61e^{-0.73\epsilon_0}\right)$$

$$H_a = \Phi\left[\left(\frac{1 - 0.5C_{ra}}{1 - C_{ra}}\right)(1 + k)\tilde{\omega}_a\right]^{0.67} \tilde{\zeta}^{\,0.53} \, \tilde{\rho}_{eqax}^{\,0.134} \, \mathfrak{R}_a^{\,0.201} \left(1 - 0.61e^{-0.73\epsilon_a}\right)$$

$$H_b = \Phi\left[\left(\frac{1 - 0.5C_{rb}}{1 - C_{rb}}\right)(1 + k)\tilde{\omega}_b\right]^{0.67} \tilde{\zeta}^{\,0.53} \, \tilde{\rho}_{eqbx}^{\,0.134} \, \mathfrak{R}_b^{\,0.201} \left(1 - 0.61e^{-0.73\epsilon_a}\right) \tag{3.60}$$

$$H_2 = \Phi\left[\left(\frac{1 - 0.5C_{r2}}{1 - C_{r2}}\right)(1 + k)\tilde{\omega}_2\right]^{0.67} \tilde{\zeta}^{\,0.53} \, \tilde{\rho}_{eq2x}^{\,0.134} \, \mathfrak{R}_2^{\,0.201} \left(1 - 0.61e^{-0.73\epsilon_2}\right)$$

where $\Phi = 2.69 \left(\frac{\pi}{6}\right)^{-0.067}$ and $\tilde{\zeta} = \frac{z_1}{\tilde{c}_p} ln\left(\frac{\eta_0}{\eta_\infty}\right)$. Finally, we are able to estimate the traction and spin coefficients. Relations from (3.63) to (3.66) define traction coefficients as the ratio between the force acting on the rolling direction and the normal force in the contact region. The tangential force is express by means of shear stress in rolling direction as:

$$dF_{Si} = \tau_{Six}dA = \tau_{Six}dxdy; \qquad\qquad i = \{0, a, b, 2\} \tag{3.61}$$

While, according the relations from (3.67) to (3.70), the spin torque is evaluated as:

$$dT_{SPi} = \left(\tau_{Siy}x - \tau_{Six}y\right)dxdy; \qquad\qquad i = \{0, a, b, 2\} \tag{3.62}$$

Combining (3.63) to (3.70) with (3.61) and (3.62), we are able to define traction and spin coefficients as follow:

$$\mu_0 = \tilde{a}_{X0}\tilde{a}_{Y0} \int_0^1 dR \int_0^{2\pi} \tilde{\tau}_{S0x}Rd\psi \tag{3.63}$$

$$\mu_a = \tilde{a}_{Xa}\tilde{a}_{Ya} \int_0^1 dR \int_0^{2\pi} \tilde{\tau}_{Sax}Rd\psi \tag{3.64}$$

$$\mu_b = \tilde{a}_{Xb}\tilde{a}_{Yb} \int_0^1 dR \int_0^{2\pi} \tilde{\tau}_{Sbx}Rd\psi \tag{3.65}$$

$$\mu_2 = \tilde{a}_{X2}\tilde{a}_{Y2} \int_0^1 dR \int_0^{2\pi} \tilde{\tau}_{S2x}Rd\psi \tag{3.66}$$

$$\chi_0 = \frac{\tilde{a}_{X0}\tilde{a}_{Y0}}{\mathfrak{R}_0\tilde{r}_0} \int_0^1 dR \int_0^{2\pi} \phi_0(\psi)R^2 d\psi \tag{3.67}$$

$$\chi_a = \frac{\tilde{a}_{Xa}\tilde{a}_{Ya}}{\mathfrak{R}_a\tilde{r}_a} \int_0^1 dR \int_0^{2\pi} \phi_a(\psi)R^2 d\psi \tag{3.68}$$

$$\chi_b = \frac{\tilde{a}_{Xb}\tilde{a}_{Yb}}{\mathfrak{R}_b\tilde{r}_b} \int_0^1 dR \int_0^{2\pi} \phi_b(\psi)R^2 d\psi \tag{3.69}$$

$$\chi_2 = \frac{\tilde{a}_{X2}\tilde{a}_{Y2}}{\mathfrak{R}_2\tilde{r}_2} \int_0^1 dR \int_0^{2\pi} \phi_2(\psi)R^2 d\psi \tag{3.70}$$

where $\phi_i(\psi) = (\tilde{\tau}_{Siy}cos(\psi) - \tilde{\tau}_{Six}sin(\psi))$, $\tilde{\tau}_{Six}$ and $\tilde{\tau}_{Siy}$ are respectively, the shear stress along the rolling direction and along the normal direction for each point of contact. $\mathfrak{R}$ is the load factor that depends on the geometry and the normal force. $\tilde{a}_X$ and $\tilde{a}_Y$ are the axes length of the elliptic contact in dimensionless form.

3.5 Simulation results

The aim of the proposed model is to evaluate the efficiency of a planetary CVT. To perform a simulation of the model, it is necessary a set of geometrical quantities, the fluid properties and the operative point of the transmission. Table 3.1 contains the geometrical quantities of the considered transmission. To analyse the creep and spin effect the efficiency results are provided in terms of speed and torque efficiency as function of the input torque at different reduction ratio. The fluid properties considered

| Aspect ratio	$k = 1.5$
Roller radius	$r_b = 0.03m$
Half cone angle disk0-roller	$\theta_0 = 45°$
Half cone angle disk2-roller	$\theta_2 = 45°$
Half cone angle idle disks-roller	$\alpha = 10°$

Table 3.1: Geometrical parameters

for this model are the same of the model developed by [24]. In this simulation the input speed has been chosen equal to $\omega_0 = 2000rpm$, while output torque ranges between $[0.01 - 12]kW$. Finally, clamping forces are chosen in order to obtain $F_{N0} = 2.5kN$.

The curves in Fig. (3.6) show the speed efficiency of the transmission. These curves show that the speed efficiency decreases at high torque. This is due to the high creep
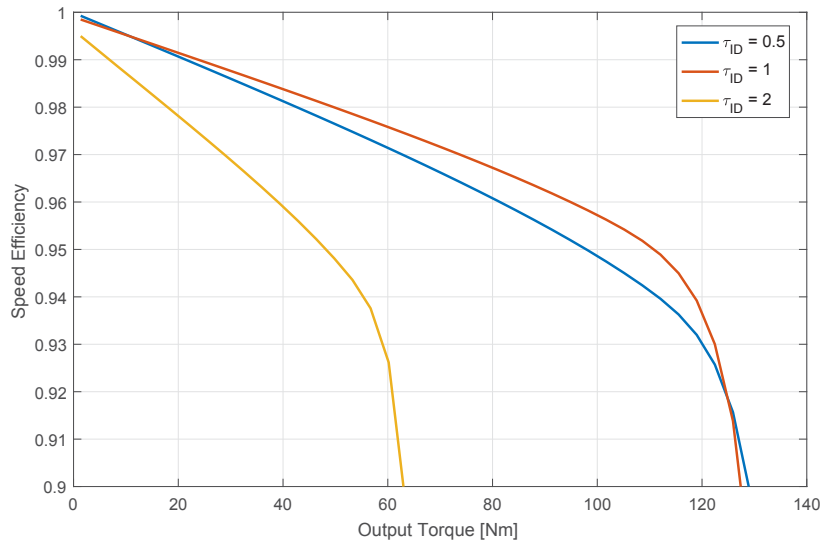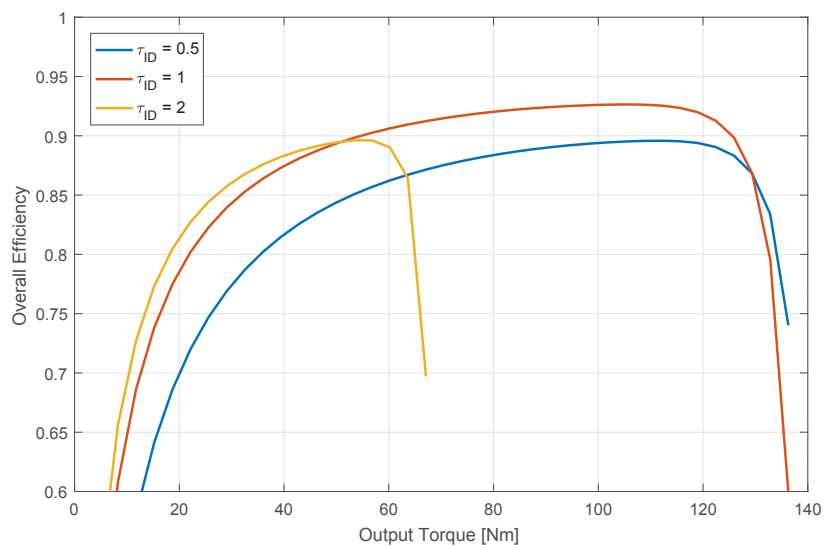
Figure 3.6: Speed efficiency as a function of output torque at different transmission ratio

necessary to generate the tangential forces in the rolling direction. Obviously, high slip produces a high losses in terms of speed efficiency. In Fig. (3.7) we can observe the losses in terms of torque. Comparing these curves with Fig. (3.17), (3.18), (3.19) and (3.20), we can observe that the higher is the transmission ratio, the higher are the spin coefficients. Due to the duality between creep losses and spin losses, the overall efficiency has the behaviour shown Fig. (3.8). In the middle part of the operative region, the efficiency is around then 90%.
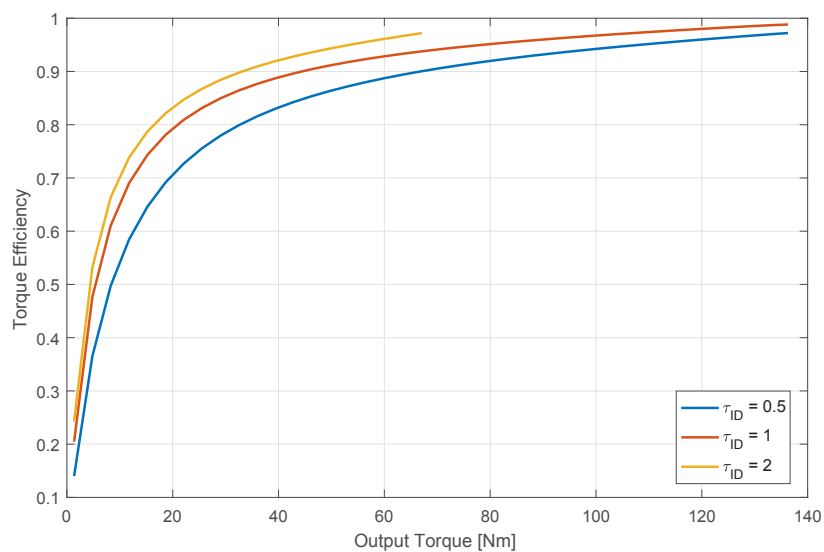
Figure 3.7: Torque efficiency as a function of output torque at different transmission ratio


**Figure 3.8:** Efficiency as a function of output torque at different transmission ratio
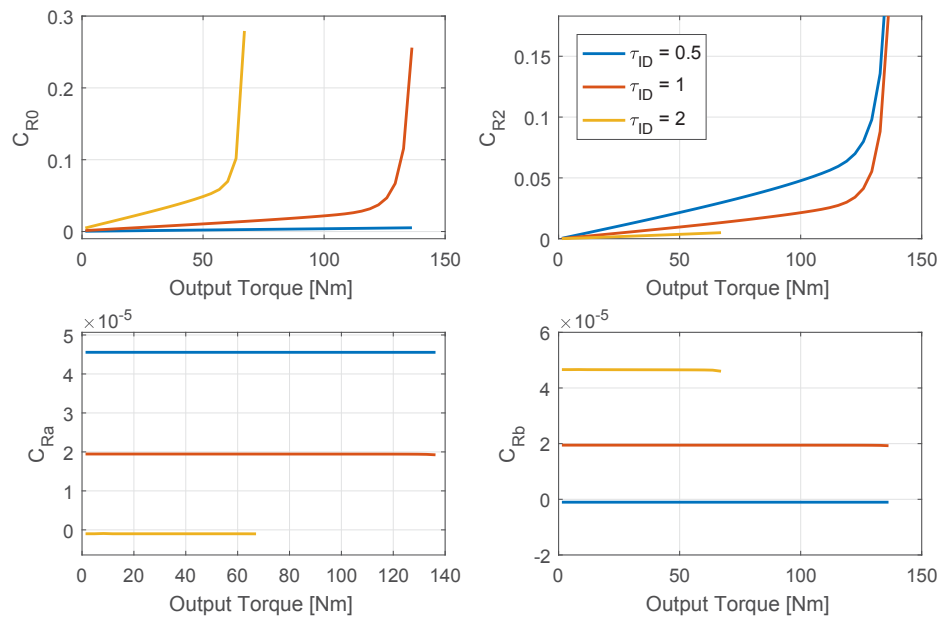
Figure 3.9: Creep coefficients as a function of output torque at different transmission ratio

As shown in Fig. (3.9), creep coefficients can assume negative values. To better understand this phenomena, we need to evaluate these coefficients through the reduction ratio range for a given operative point. Fig. (3.10) and Fig. (3.11) show creep and spin coefficients as function of transmission ratio considering $\omega_0 = 2000 rpm$ and $T_2 = 40 Nm$. This evaluation shows that negative creep may occur when the spin velocity changes in sign. Considering (3.31) and (3.33), the torques acting on the sun shafts are due to the combination of spin and creep effects and, obviously, also to the torque due to the bearing losses. When spin changes in sign, the torque equilibrium on the shafts is may produce a change in sign also for the torque due to the creep effect. It is worth noting that, for a given geometry of the transmission, this effect is emphasized for low values of bearing friction because the spin effect became comparable with the friction torque.
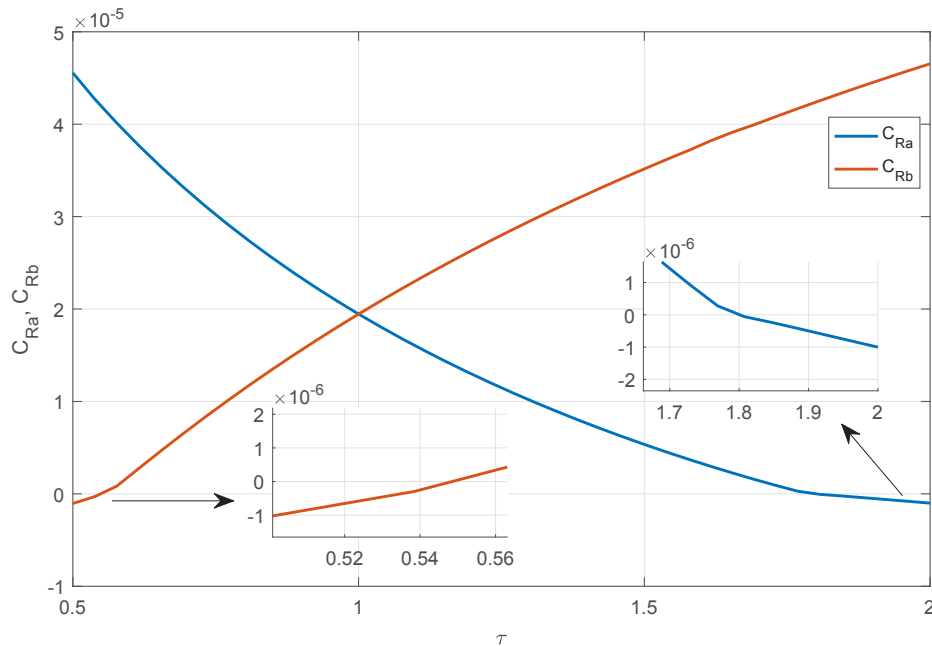
Figure 3.10: Creep coefficients as a function of transmission ratio

As result of this effect, the tangential speed of the sun shafts became higher than the tangential speed of the roller in the contact region. Obviously, this doesn't mean that the power flow from the shafts to the roller. Considering that the presented model
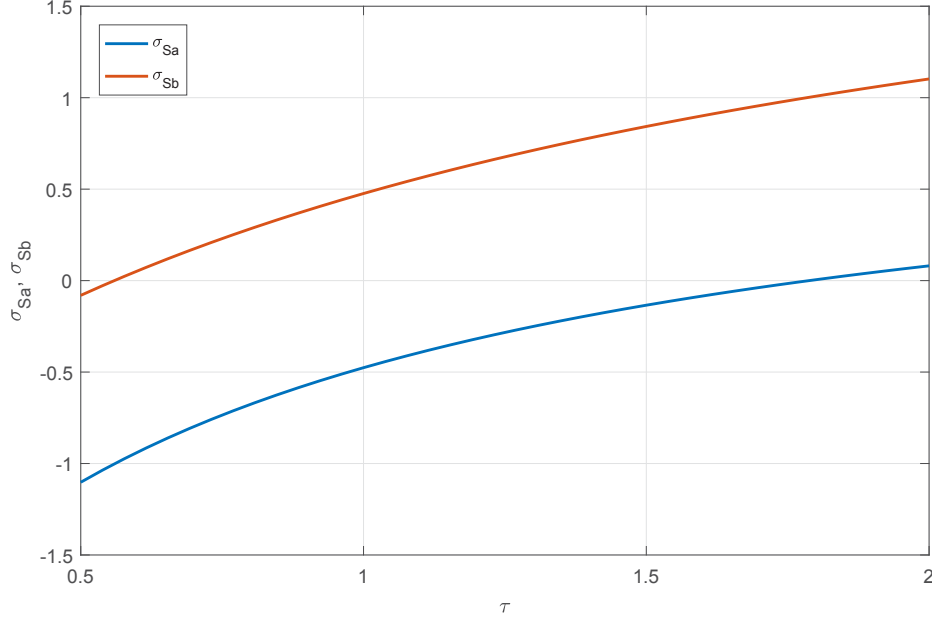
Figure 3.11: Spin coefficients as a function of transmission ratio

take in account creep, spin and friction losses, following relation hold true:

$$P_{CR} = n \left(|\omega_0 r_0 C_{R0} F_{S0}| + |\omega_S r_{Sa} C_{Ra} F_{Sa}| + |\omega_S r_{Sb} C_{Rb} F_{Sb}| + |\omega_S r_{S2} C_{R2} F_{S2}| \right)$$

$$P_{SP} = n \left(|T_{SP0} \sigma_{S0} \omega_0| + |T_{SPa} \sigma_{Sa} \omega_a| + |T_{SPb} \sigma_{Sb} \omega_b| + |T_{SP2} \sigma_{S2} \omega_2| \right)$$

$$P_{BL} = n \left(|T_{SBL} \omega_S| + |T_{BLa} \omega_a| + |T_{BLb} \omega_b| \right) \tag{3.71}$$

$$P_{loss} = P_{CR} + P_{SP} + P_{BL}$$

where P_{loss} is the global power losses in the transmission. Using its definition, the overall efficiency can be evaluated follow:

$$\eta = 1 - \frac{P_{loss}}{P_0} = 1 - \frac{P_{loss}}{T_0 \omega_0} \tag{3.72}$$

Differently from (3.44), where the efficiency is evaluated considering the input and output power, the relation in (3.72) take in account every losses considered by the model. Fig. (3.12) shows that both the methods to evaluate the efficiency produce the same result, even if the creep coefficient changes in sign. As stated before, the change
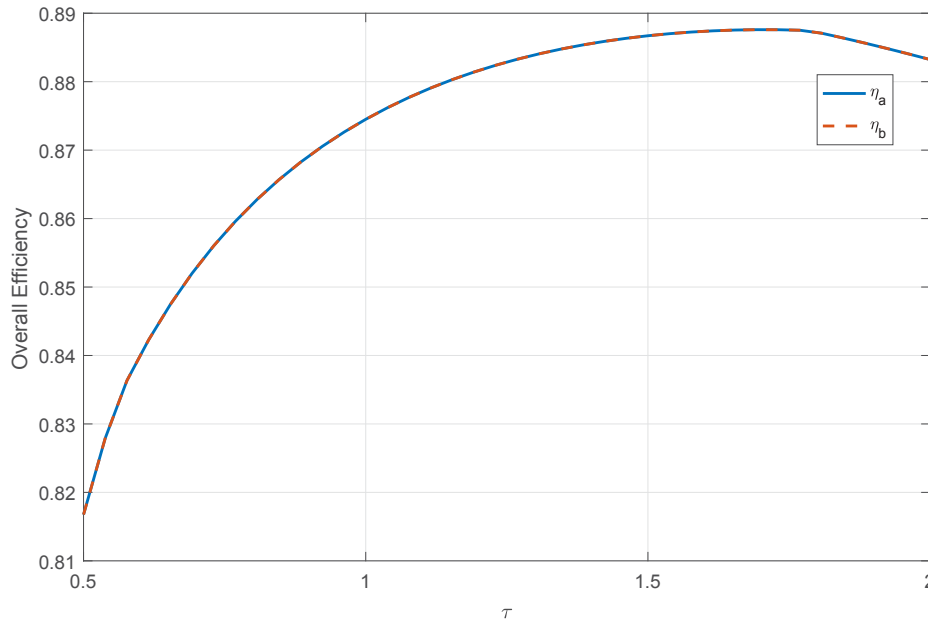
Figure 3.12: η_a Efficiency as function of transmission ratio using (3.44) - η_b Efficiency as function of transmission ratio using (3.72)

in sign of the creep coefficient is due to the change in sign of the spin coefficient. It is worth noting to verify what happen if the two sun shafts are substituted by a single shaft as show in Fig. (3.13). Obviously, in this case the spin torque does not act on the sun shaft. Fig. (3.14)

Finally, Fig. (3.15) shows the difference in terms of efficiency between the single sun shaft version and the CVT considered in this work. The single shaft version presents an efficiency peak for $\tau = 1$, moreover is globally higher then the considered CVT. This difference is due to the additional losses in terms of creep, spin and friction.

3.6 Contribution

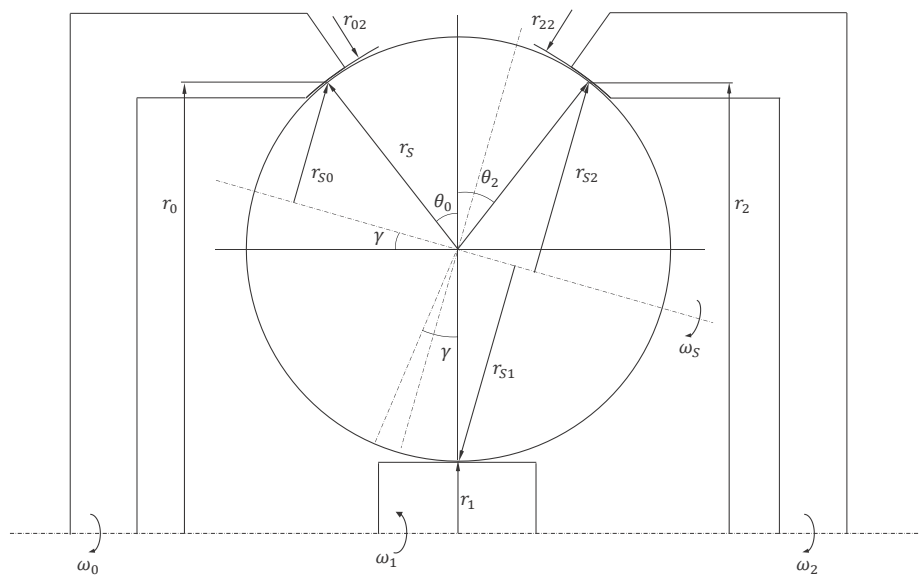The work described in this chapter has been published in [27] and [28].

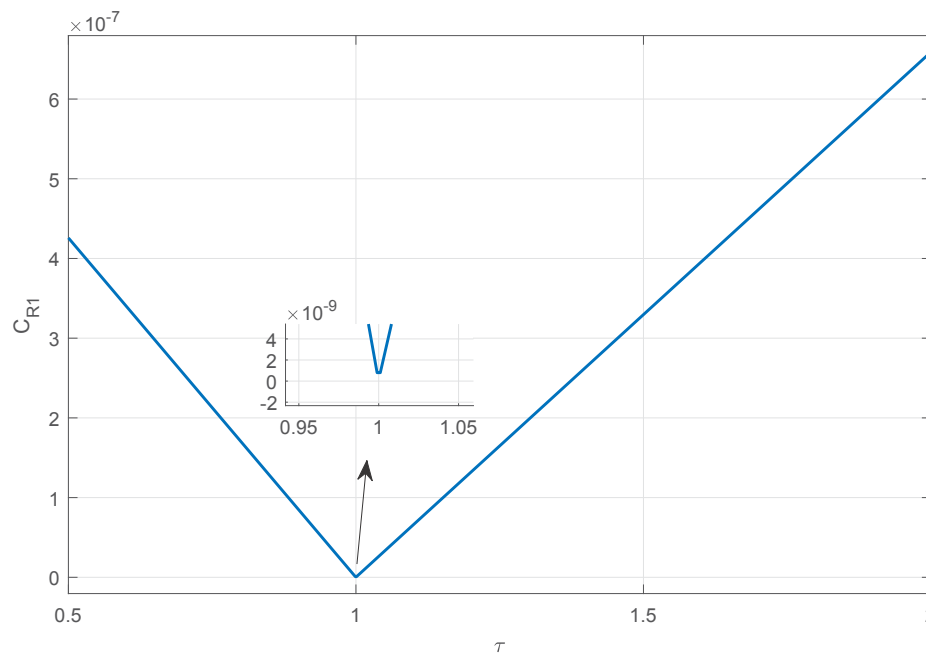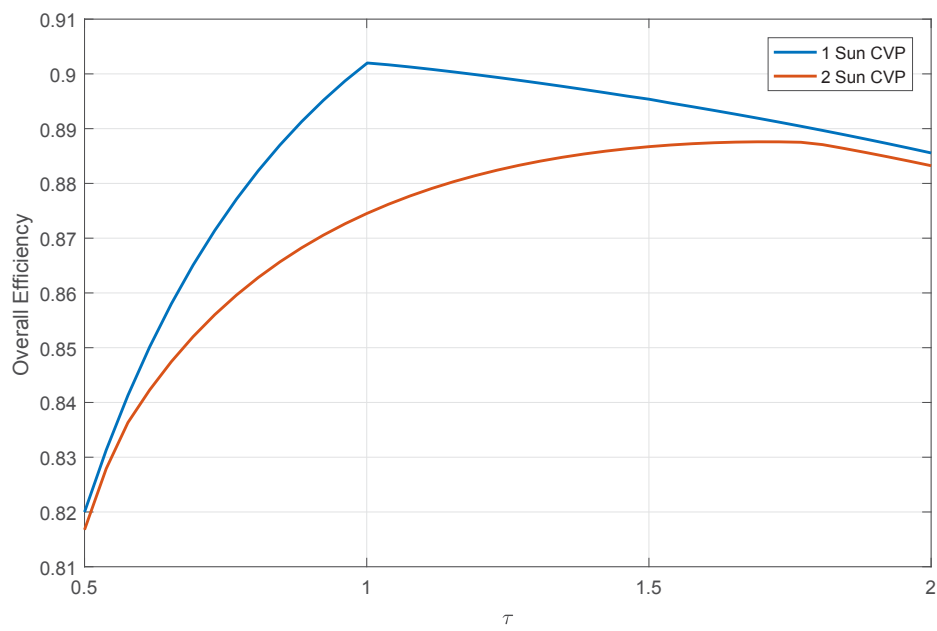**Figure 3.13:** CVT Geometrical quantities with a single sun shaft

Figure 3.14: Creep coefficient on the single sun shaft as a function of transmission ratio

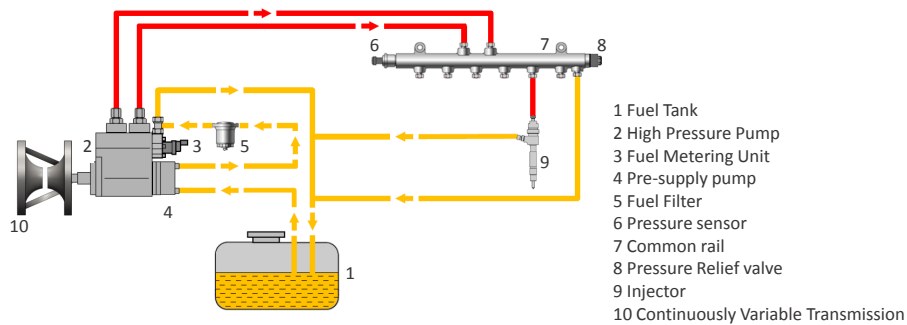**Figure 3.15:** Single sun shaft Vs two sun shafts efficiency comparison

Common rail pressure control with a CVT

4.1 Proposed control strategy

The main component of the CRS is the high-pressure volumetric pump, which raises the fuel pressure to the reference value set for the common-rail. In modern systems, the common-rail pressure is regulated by adjusting the pump inlet flow using a FMU [29]. Considering that the flow delivery from a volumetric pump depends on the pump speed and on the FMU driving current, we can write the common-rail dynamic equation as follow:

$$\dot{p}_r = \frac{\beta}{V_r}(q_{pump}(I_{FMU}, p_r, \omega_p) - q_{inj} - q_{leak}) \tag{4.1}$$

where p_r is the rail pressure, V_r is the rail volume, ω_p is the high-pressure pump speed, I_{FMU} is the FMU current that, as previously stated, defines the pump incoming flow, q_{inj} is the injected flow and q_{leak} is the leakage flow from the injectors. From eq. (4.1), it is evident that the pump speed variation may be used in combination with

1 Fuel Tank
2 High Pressure Pump
3 Fuel Metering Unit
4 Pre-supply pump
5 Fuel Filter
6 Pressure sensor
7 Common rail
8 Pressure Relief valve
9 Injector
10 Continuously Variable Transmission

Figure 4.1: Common-rail injection system with a Continuously Variable Transmission
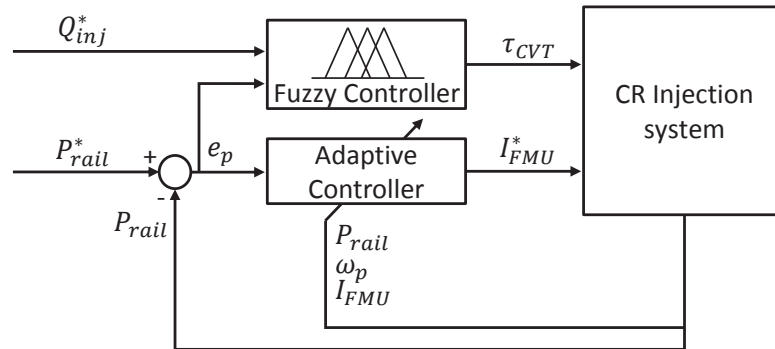
Figure 4.2: Diesel Common-rail pressure control scheme using a Continuously Variable Transmission and a Fuel Metering Unit

the control of the FMU current to regulate the delivery of the pump and thus the common-rail pressure. This new concept of CRS allows the pump to operate at a lower speed in presence of low and medium flow demands, enabling a reduction of the power needed to drive the pump. Moreover, the mechanical design of the pump and the testing phase are simplified because the overrun conditions can be avoided. The variation of the pump speed can be obtained in several ways. The more intuitive one is to drive the pump by using an electric motor, enabling precise and easy control of the pump speed. The drawback of this solution is that it requires the availability of a suitable electric motor with an adequate power supply system, resulting in an unacceptable increase of weight and size of the CRS. An alternative method to obtain the same result is the adoption of a traction drive CVT. These kind of transmissions are efficient and compact, and suitable to be used in the automotive field [27], [28]. As shown in Fig. 4.1, the CVT is mounted directly on the high-pressure pump shaft to change its speed. Besides, the pump is equipped with a FMU. Moreover, the valve guarantees a faster regulation of the common-rail pressure than the CVT, which instead aims at reducing the speed of the high-pressure pump globally.

The proposed new topology of the CRS requires an adequate control strategy. The main issue to solve in the design process is related to the presence of two actuators (i.e. the FMU and the CVT) and one controlled output. The first step to manage this

redundancy is to define the goals the actuators must achieve. Starting from the FMU, we need a fast controller that takes into account the high-pressure speed variation (in order to decouple the control loops), therefore the adaptive controller described in [30] is used to this purpose. The second control loop varies the speed ratio of the CVT to satisfy the flow demand of the injectors, without introducing any disturbances on the common-rail pressure. To achieve these goals, we develop a Fuzzy logic controller with the common-rail pressure tracking error and the flow demand as the inputs, and the speed ratio of the CVT as the output. The block scheme in Fig. 4.2 shows the layout of the control loops.

4.1.1   FMU control

Eq. (4.1) can be rewritten as follows:

$$\dot{p}_r \simeq f(I_{FMU}, p_r, \omega_p) + \xi \tag{4.2}$$

being ξ the uncertainty due to the approximation of the model. We can assume that ξ does not depend on $x = \{I_{FMU}, p_r, \omega_p\}$ [16]. Linearizing eq. (4.2) around a generic point $x_0 = \{I_{FMU0}, p_{r0}, \omega_{p0}\}$ gives the following linear model:

$$\dot{p}_r \simeq \left.\frac{\partial f}{\partial p_r}\right|_{x_0} p_r + \left.\frac{\partial f}{\partial \omega_p}\right|_{x_0} \omega_p + \left.\frac{\partial f}{\partial I_{FMU}}\right|_{x_0} I_{FMU}$$

$$\tag{4.3}$$

$$\dot{p}_r \simeq \alpha_1 p_r + \alpha_2 \omega_p + \beta_1 I_{FMU}$$

Obviously, the model parameters are unknown, $\Phi = [p_r, \omega_p, I_{FMU}]$ is supposed to be available for feedback. An estimate of this model can be obtained by:

$$\dot{\hat{p}}_r = \hat{\alpha}_1 p_r + \hat{\alpha}_2 \omega_p + \hat{\beta}_1 I_{FMU} - l_p \tilde{p}_r =$$

$$\tag{4.4}$$

$$= \Phi \hat{\chi} - l_p \tilde{p}_r$$

where $l_p > 0$ is the error estimation gain, $\hat{\chi} = [\hat{\alpha}_1, \hat{\alpha}_2, \hat{\beta}_1]^T$ is the set of parameters estimation, and $\tilde{p}_r = \hat{p}_r - p_r$ is the estimation error. By comparing (4.3) and (4.4), we can write the estimation error dynamics as follows:

$$\dot{\tilde{p}}_r = \Phi \tilde{\chi} - l_p \tilde{p}_r - \xi \tag{4.5}$$

where $\tilde{\chi} = \hat{\chi} - \chi$ is the parameter estimation error. Our goal is to find an adaptation law for $\hat{\chi}$ in order to minimize $\tilde{\chi}$ and $\tilde{p}_r$. For this purpose, we can define the following candidate Lyapunov function:

$$V(\tilde{p}_r, \tilde{\chi}) = \frac{1}{2}\tilde{p}_r^2 + \frac{1}{2\gamma}\tilde{\chi}^T \tilde{\chi} \tag{4.6}$$

where $\gamma > 0$. This function is positive-definite in the origin, while the time-derivative of this function is:

$$
\begin{aligned}
\dot{V}(\tilde{p}_r, \tilde{\chi}) &= \frac{\partial V}{\partial \tilde{p}_r}\dot{\tilde{p}}_r + \frac{\partial V}{\partial \tilde{\chi}}\dot{\tilde{\chi}} = \\
&= \tilde{p}_r \Phi \tilde{\chi} - l_p \tilde{p}_r^2 - \xi \tilde{p}_r + \frac{\dot{\tilde{\chi}}^T \tilde{\chi}}{\gamma} = \\
&= \left[\tilde{p}_r \Phi + \frac{\dot{\tilde{\chi}}^T}{\gamma}\right]\tilde{\chi} - l_p \tilde{p}_r^2 - \xi \tilde{p}_r
\end{aligned}
\tag{4.7}
$$

Since $\tilde{\chi} = \hat{\chi} - \chi$, and χ is constant, we can define the adaptation law as follows:

$$
\dot{\hat{\chi}} =
\begin{bmatrix}
\dot{\hat{\alpha}}_1 \\
\dot{\hat{\alpha}}_2 \\
\dot{\hat{\beta}}_1
\end{bmatrix}
= -\gamma \Phi^T \tilde{p}_r = -\gamma
\begin{bmatrix}
p_r \\
\omega_p \\
I_{FMU}
\end{bmatrix}
\tilde{p}_r
\tag{4.8}
$$

Thus, the time derivative of the candidate Lyapunov function (4.7) becomes:

$$\dot{V}(\tilde{p}_r, \tilde{\chi}) = -l_p \tilde{p}_r^2 - \xi \tilde{p}_r \tag{4.9}$$

We can note that while $\tilde{p}_r$ increases, the value of the candidate Lyapunov function decreases. Due to the presence of $\xi \tilde{p}_r$, we can take the error bounded but not converging

to zero. Once the model estimation is near to the actual value of the common-rail pressure, we can use eq. (4.4) to design a control law for the system. We consider the following second-order reference model in a state space representation:

$$
\begin{bmatrix} \dot{p}_{ref} \\ \ddot{p}_{ref} \end{bmatrix} = \begin{bmatrix} 0 & 1 \\ -\omega_n^2 & -2\delta\omega_n \end{bmatrix} \begin{bmatrix} p_{ref} \\ \dot{p}_{ref} \end{bmatrix} + \begin{bmatrix} 0 \\ \omega_n^2 \end{bmatrix} p_r^* \tag{4.10}
$$

where p_r^* is the desired rail pressure, and p_{ref} is the model reference output. We can define the tracking error as $\tilde{e}_p = \hat{p}_r - p_r$, and the tracking error dynamics as follows:

$$
\dot{\tilde{e}}_p = \varphi - \dot{p}_{ref} + \hat{\beta}_1 I_{FMU} \tag{4.11}
$$

where $\varphi = \hat{\alpha}_1 p_r + \hat{\alpha}_2 \omega_p - l\tilde{p}_r$. From this equation, we can derive the control law in order to obtain the desired behavior of the tracking error. Let the desired dynamics be described by $\dot{\tilde{e}}_p = -k_p \tilde{e}_p$, the obvious choice for the solenoid current reads as follows:

$$
I_{FMU} = \frac{1}{\hat{\beta}_1} \left[\dot{p}_{ref} - \varphi - k_p \tilde{e}_p \right] \tag{4.12}
$$

where $k_p > 0$. The energizing current that can flow through the electrical circuit of the FMU has minimum and maximum thresholds. To consider this constraints without having windup issues, we need to consider the actuator saturation in the control law definition. The saturation can be express as:

$$
\bar{I}_{FMU} = \begin{cases} I_{FMUmin} & I_{FMUmin} < I_{FMU} \\\\ I_{FMU} & Otherwise \\\\ I_{FMUMax} & I_{FMU} > I_{FMUMax} \end{cases} \tag{4.13}
$$

Consequently, to consider the saturation of FMU energizing current the estimation equation and the tracking error dynamic are rewritten as follows:

$$\dot{\hat{p}}_r = \Phi(p_r, \omega_p, \bar{I}_{FMU})\hat{\chi} - l_p\tilde{p}_r \tag{4.14}$$

$$\dot{\tilde{e}}_p = \varphi - \dot{p}_{ref} + \hat{\beta}_1\bar{I}_{FMU} \tag{4.15}$$

4.1.2   CVT control

The goal of the CVT control system is to regulate the high-pressure pump speed according to the flow demand and the common-rail pressure tracking error. To most intuitive way to reach this result is the adoption of a Fuzzy Logic Controller. Thus, we can start designing this controller by defining the following fuzzy sets for the flow demand and the transmission ratio: VL = *Very Low*; L = *Low*; M = *Middle*; H = *High*; VH = *Very High*. The fuzzy set for the tracking error is: VN = *Very Negative*; N = *Negative*; Z = *Zero*; P = *Positive*; VP = *Very Positive*. Once the fuzzy sets are defined, we can assign the membership functions to the normalized input and output variables. According to the experience and the physical behavior of the system under study, we consider the membership functions in Fig. 4.3 and Fig.4.4. In particular, we can observe that the *lower* side of the transmission ratio range is more dense with respect to the *higher* side. This design choice, together with the rule table defined in Tab. 4.1, helps to reduce the high-pressure pump speed according to the flow demand. The resulting control surface of the fuzzy controller is depicted in Fig. 4.5. Due to design limitations, the high-pressure pump speed is bounded between a maximum and a minimum value. The former limit results from the robustness of the high-pressure pump components. Given that the considered pump is fuel lubricated, the lower limit is related to the minimum lubrication of the pump bushing bearings, and is a function of the common-rail pressure. Obviously, the CVT functioning limits must be considered in the control loop too. In the out system, we are considering a CVT ratio that ranges in the interval $0.5 \leq \tau_{CVT} \leq 3$, so we can write the pump speed

$$\tilde{Q}^*_{inj}$$

|	τ_{CVT}	VL	L	M	H	VH
	VN	VL	VL	VL	L	L
	N	VL	VL	L	L	M
$\tilde{e}_p$	**Z**	VL	L	M	M	H
	P	L	M	M	H	VH
	VP	M	M	H	H	VH

Table 4.1: Fuzzy controller rules table

limitations as follows:

$$max(\tau_{min}\omega_e, \omega_{pMin}(p_r)) \leq$$

$$\leq \omega_p \leq \qquad (4.16)$$

$$\leq min(\tau_{Max}\omega_e, \omega_{pMax})$$

where ω_e is the engine speed, ω_{pMax} is the maximum pump speed, while τ_{min} and τ_{Max} are respectively the lower and higher transmission ratios of the CVT.

4.1.3   Simulation results

In this section, we show some simulation results to assess the validity of the proposed topology and control method. The simulation is performed in Matlab & Simulink in transient conditions, by considering a driving cycle directly derived from the WHTC driving cycle for heavy-duty vehicles. A comparison is performed between the new topology and the traditional CRS equipped with the FMU and the controller described in Section 4.1.1. As previously stated, the results are partially normalized to meet the company agreements. In particular, the high-pressure pump speed is normalized with respect to the maximum value, while the power demand is normalized with respect a common value between the two topologies, in order to guarantee the comparability of the results.
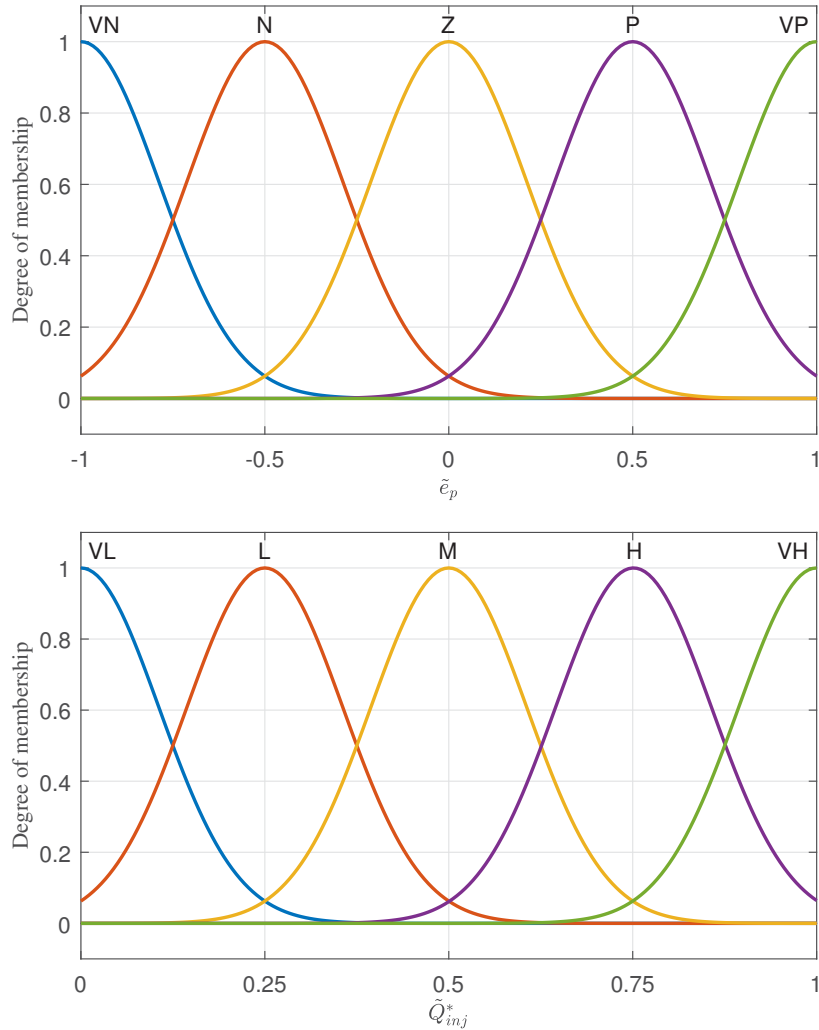
Figure 4.3: Input variables membership functions

First of all, it is verified that the tracking performance of the proposed control strategy, combining the FMU and the CVT, are comparable with those obtained with the traditional topology, as shown in Fig. 4.6. It is worth remembering that the main goal of the new topology is the reduction of the high-pressure pump speed. From Fig. 4.7, we can observe that the introduction of the CVT globally lowers the pump speed, where Fig. 4.8 shows the transmission ratio reached during the simulation.

To better analyze the controlled system performance, we can evaluate the high-pressure pump speed density and cumulative functions. Fig. 4.10 shows the drastic reduction of the speed. In particular, we can observe that 90% of the pump speed values reached
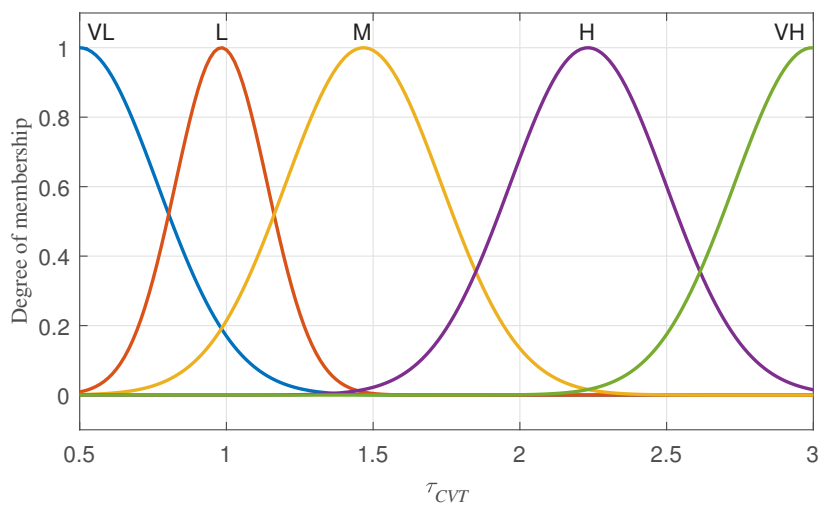
Figure 4.4: Output variables membership functions

with the traditional topology range between 36% and 76% of the maximum value, while this range changes to 28% and 59% with the new topology.

Finally, Fig. 4.9 shows the power demand reduction. The depicted results are normalized by adopting the same procedure in both cases, and consider only the mechanical power required to drive the pump. Having the same flow demand and pressure in the pump cylinder, the hydraulic power is almost equivalent for the two topologies.

4.2 Contribution

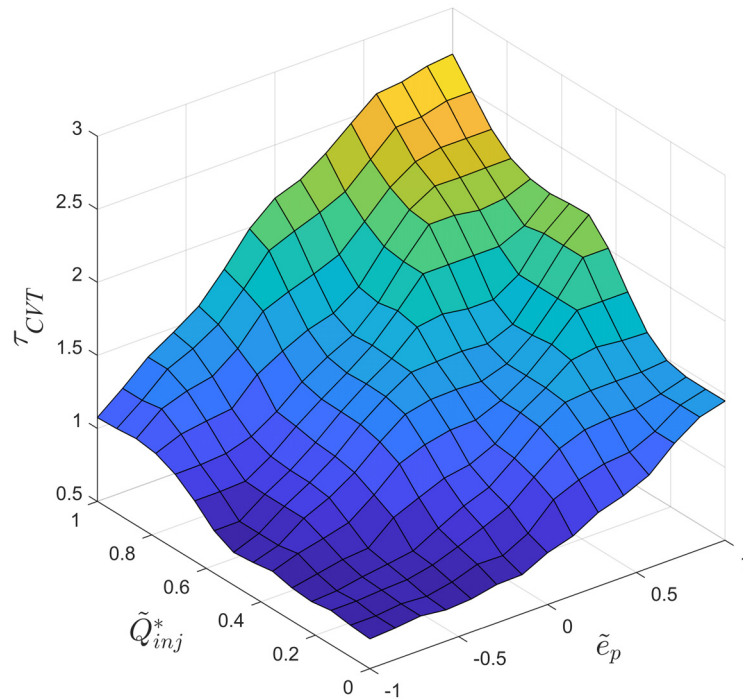The results shown in this chapter have been published in [31].
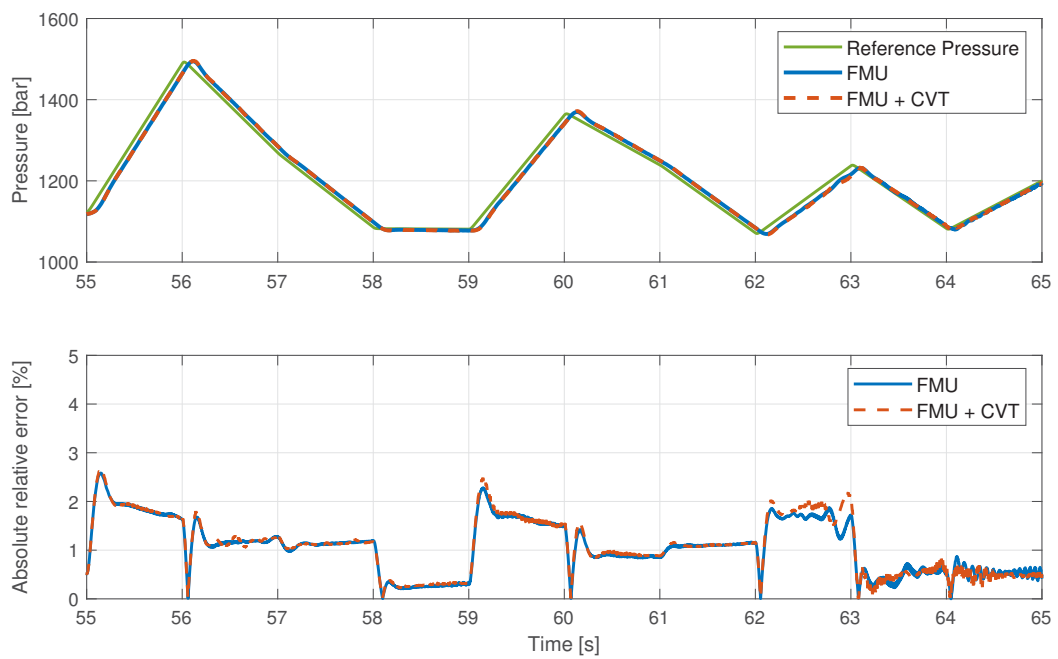
Figure 4.5: Fuzzy control surface

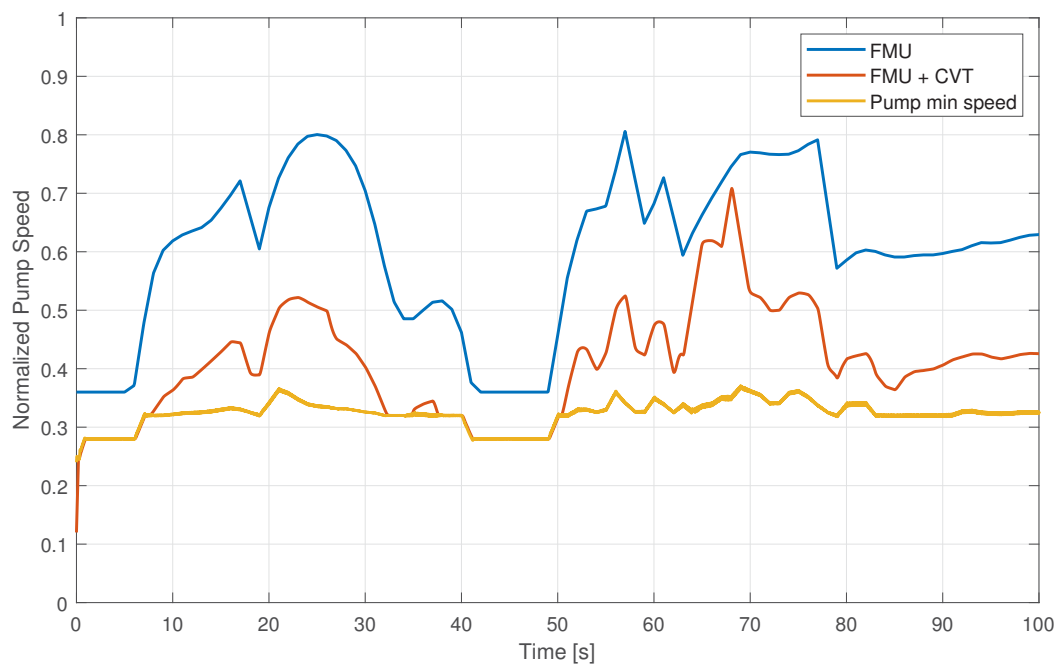

Figure 4.6: Tracking performance comparison

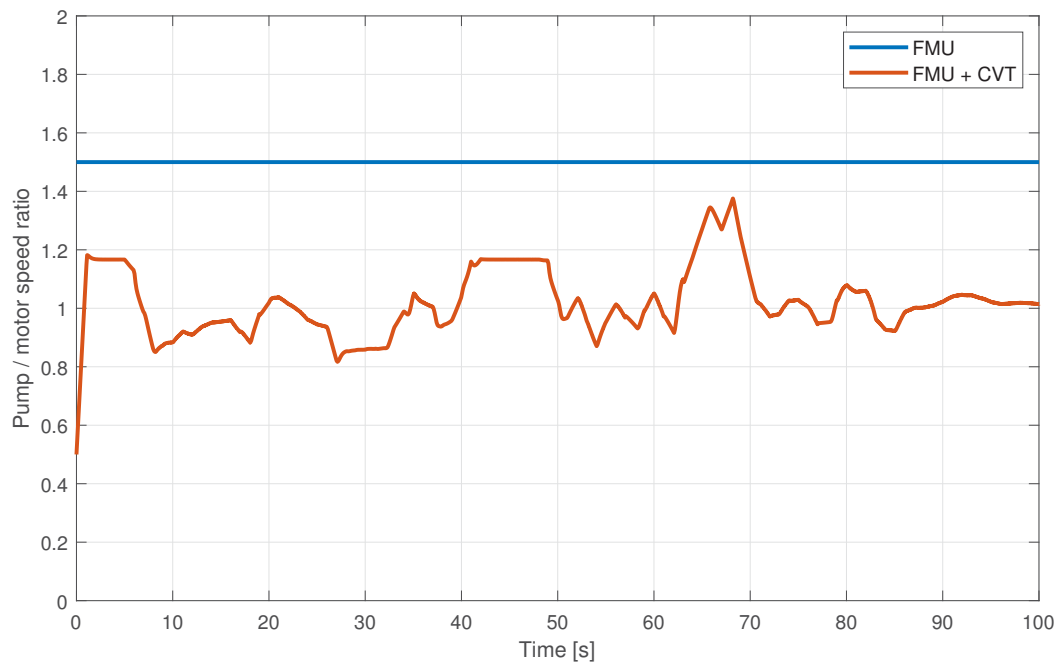**Figure 4.7:** Normalized high-pressure pump speed comparison

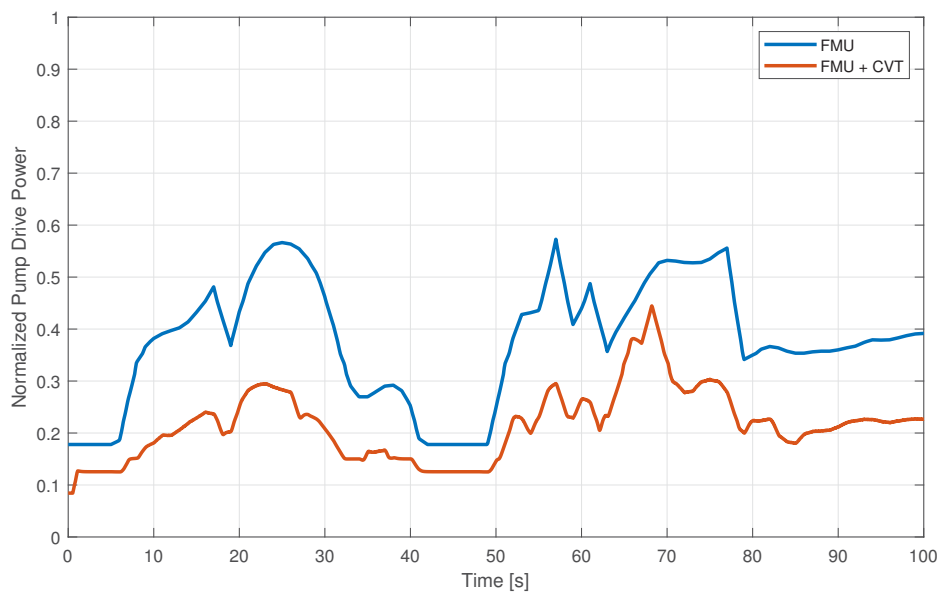**Figure 4.8:** CVT ratio - Evaluated as Pump speed / Engine speed

Figure 4.9: Mechanical Power demand required to drive the high-pressure pump
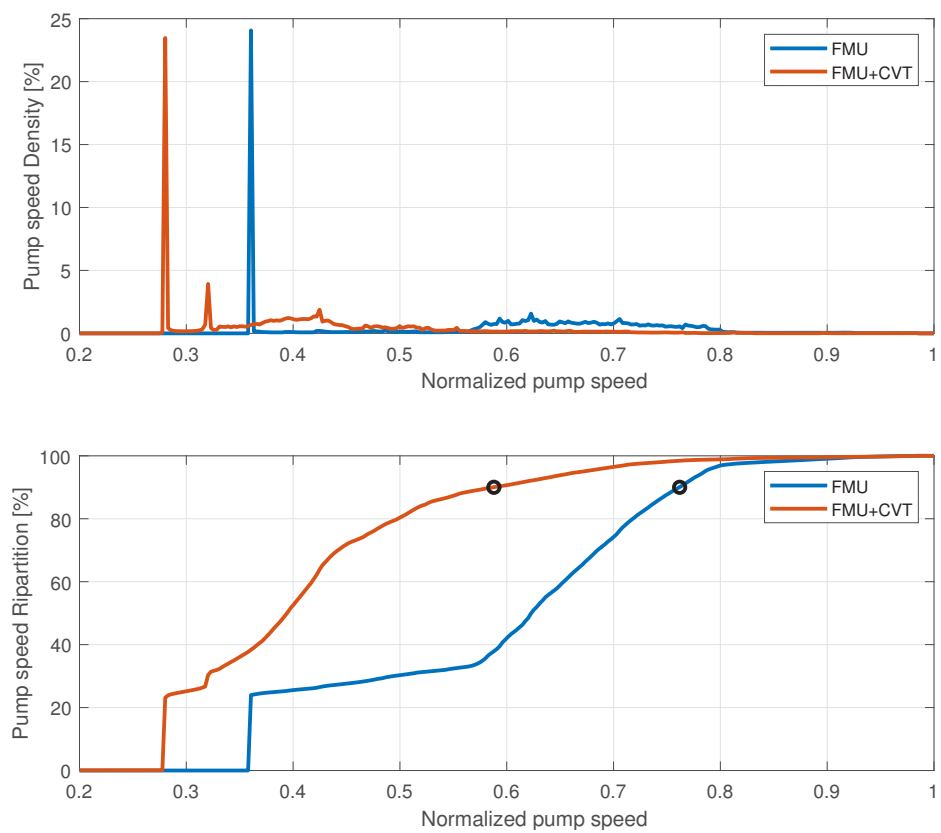

Figure 4.10: High-pressure speed analysis. Speed density function (TOP) and Speed cumulative function (bottom)

CHAPTER 5

Proof of concept validation

5.1 Test bench description

The development of the experimental set-up has the objective to assess the feasibility and effectiveness of this new topology and of its application to CRS. Fig. 5.1 depicts the layout of the test bench which replicates the real one in Fig. 4.1. For this test, an external gear pump is used in place of the high pressure piston pump, while the CVT comes from the bike market, where is usually sold under the trade name *NuVinci*. In this transmission, the speed ratio is changed by moving a geared shaft beside the input shaft. Normally, this actuation is made manually using a knob on the handlebar, while in the proposed experiment is performed by a servo motor. A solenoid valve substitutes the injectors to simulate a controllable flow demand. Finally, to protect the components against faults, a safety valve is mounted between the outlet port of the gear pump and the tank to automatically limit the pressure under a specified value ($\Delta p_{open} \sim 12bar$). The pump outlet pressure is regulated by varying the pump speed. This is obtained by implementing the control scheme depicted in Fig. 5.2. In particular, a PI is used to define the servo motor position according to the tracking error between the reference pressure and the actual pressure that is sensed with a piezoelectric sensor placed between the pump ant he valves. The solenoid valve opening is obtained by setting the PWM duty cycle.

As previously mentioned, the test-bench includes a CVT traction drive known as *NuVinci* for commercial application. As explained in Ch. 3, this kind of transmissions exploit a so called *traction oil* to transmit the power through the input and output
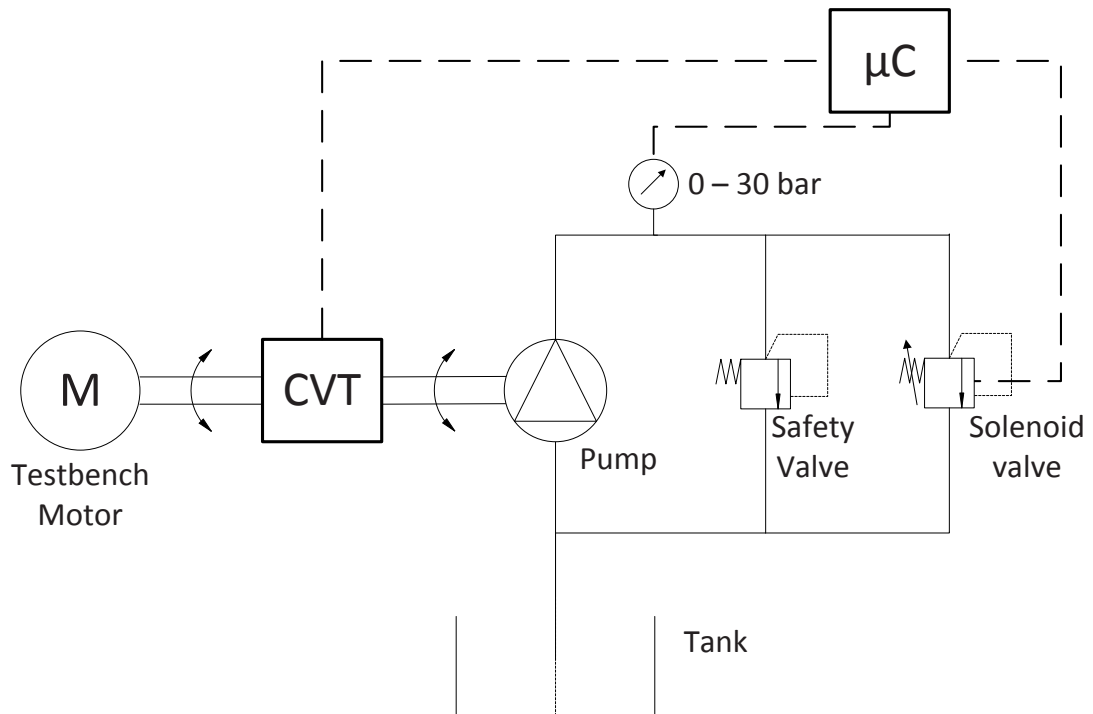
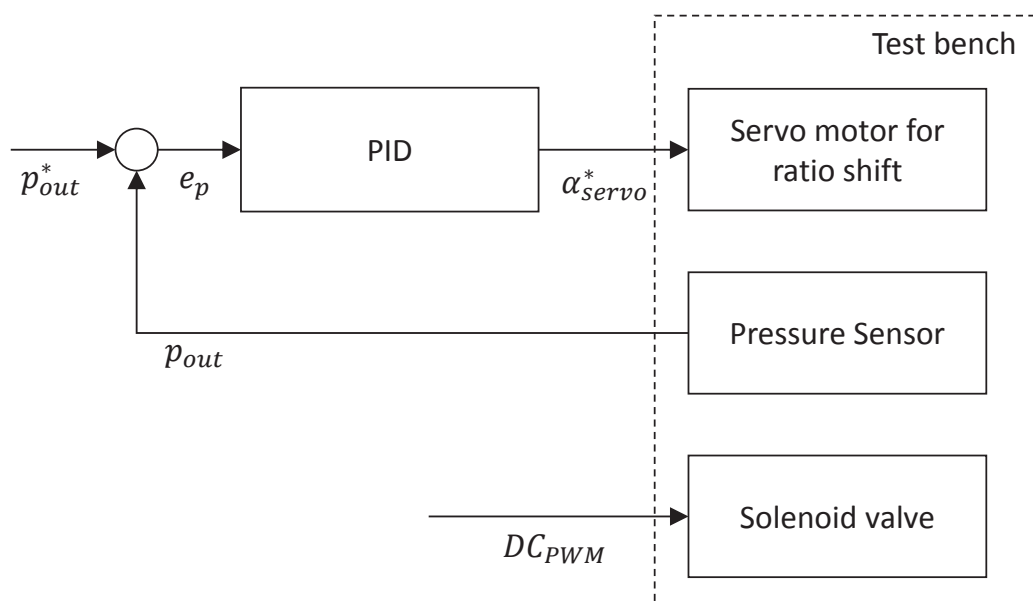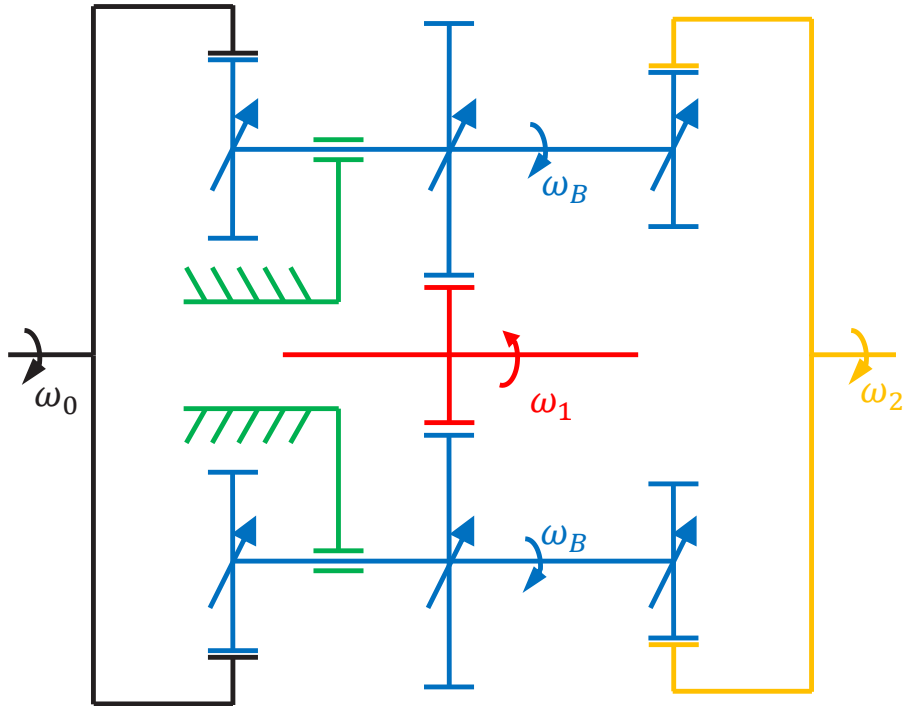**Figure 5.1:** Test bench layout

Figure 5.2: Control Scheme

**Figure 5.3:** Analogy with a two stage planetary gearset

shaft. Due to its physical properties, the viscosity of the traction oil increases under high contact pressure. In this way, there is no need for belts, chains or teeth meshing. Without these mechanical constraints, the transmission ratio can be adapted by acting on the angle between the axes of rotation of internal parts of the transmission.

By comparing Fig. 3.1 and Fig. 5.3, it's easy to see that for each value of γ, the CVT can be analysed as a two-stage planetary transmission [27], [28]. The evaluation of the overall speed ratio can be performed comparing the tangential speed in the point of contact. In ideal conditions, the following relations hold true:

$$\omega_0 r_0 = \omega_B r_{B0}$$

$$\omega_2 r_2 = \omega_B r_{B2}$$

(5.1)

where ω_0 is the input shaft speed, ω_B is the speed of the rollers, and ω_2 is the output shaft speed. Using the analogy with a two stage planetary gears and the geometrical
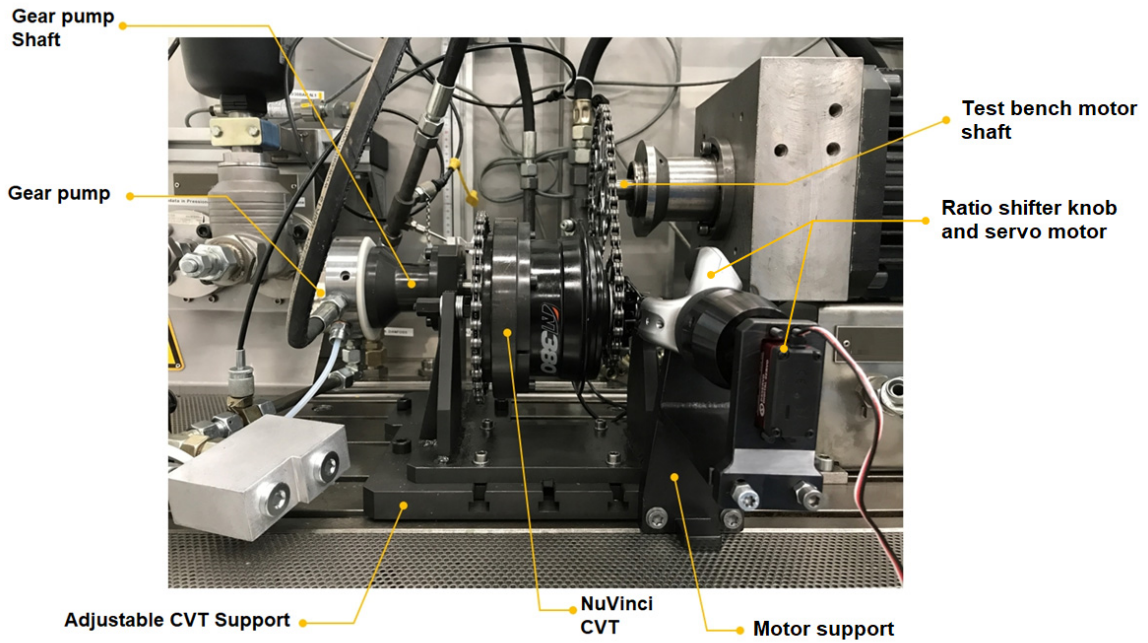
**Figure 5.4:** Test bench used for the proof of concept validation

quantities of the transmission, it is easy to see that by assuming $\theta_0 = \theta_2 = \theta$, the speed ratio becomes:

$$\tau = \frac{\omega_2}{\omega_0} = \frac{cos(\theta - \gamma)}{cos(\theta + \gamma)} \tag{5.2}$$

5.2   Experimental results

The proposed proof of concept has been implemented on a real test bench which is normally used for gear pump tests. Fig. 5.4 shows a front view of the test bench. In order to simplify the assembling procedure, the coupling between the CVT and the other components is obtained by using chains for bike applications. The servo motor adjusts the transmission ratio.

The control logic is implemented on an Arduino Mega 2560 board programmed within the Matlab/Simulink environment. To meet the hardware limitations, the pump outlet pressure was regulated by a discrete-time PI controller, which is typically used for injection control and usually tuned by the open-loop Ziegler-Nichols rules, by adopting
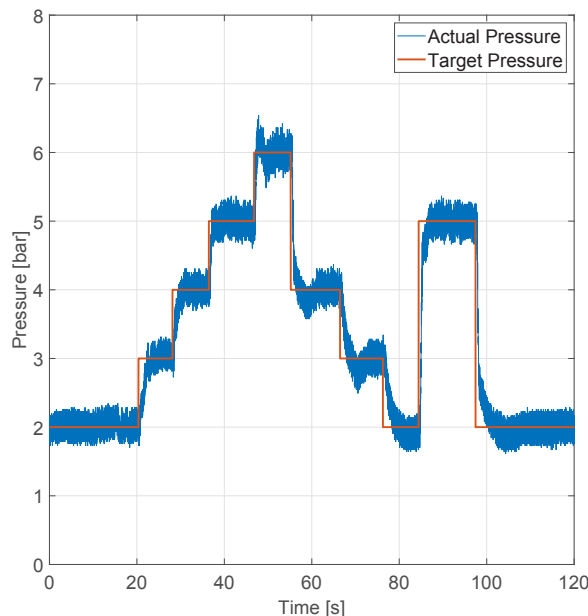
Figure 5.5: Tracking performance

a sampling-time of $T_s = 0.001s$. The servomotor is a DS3225 with 270° of displacement that meets exactly the maximum rotation of the handlebar knob of the *NuVinci*. As shown in Fig. 5.4, the servomotor is mounted directly on the knob to guarantee a fast and precise regulation of the speed ratio.

The controller is tuned by using the Ziegler-Nichols method, with a fine tuning to reduce settling time, avoiding the overshoots and pressure oscillations in steady state. These requirements comes from the real specification of a CRS in which the pressure regulation needs to be fast enough in order to provide the torque demand of the driver, while the absence of oscillations is necessary to not disturb the injection phases. As stated before, the fuel injected quantity is defined according the rail pressure and the opening time of the injector. If the rail pressure doesn't meet the target pressure, the quality of the injection deteriorates which would involve in bad combustion in the cylinder chamber. The reference signal is composed of successive pressure steps ranging within the interval [2-6] bar. Fig. 5.5 shows the tracking performances. As shown, the pressure regulation is fast, stable and precise according the requirements. As expected, during the falling of the target pressure, the system suffers the presence of the freewheel

Motor speed	150 rpm
Duty cycle solenoid valve	30 %
Target Pressure range	[2 - 6] bar
Test oil temperature	20°C
Shiter ratio angular displacement	270°
Pump Inlet pressure	1 bar

Table 5.1: Experiment conditions
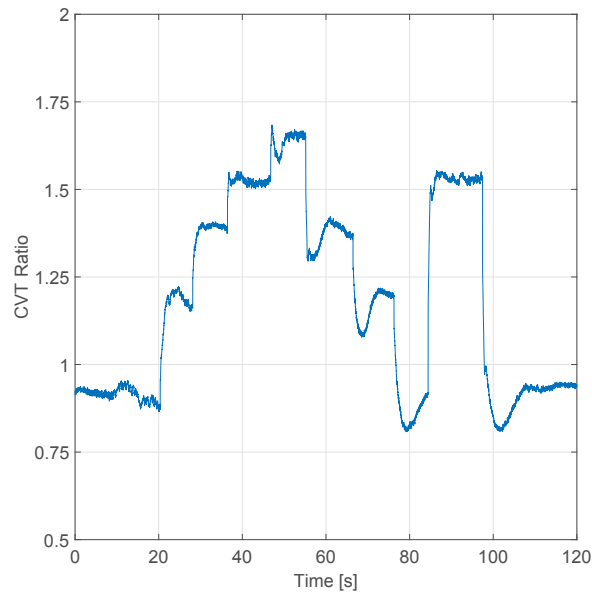
Figure 5.6: CVT speed ratio

inside the transmission that is obviously necessary in the bike applications, but is not necessary for our purposes. Fig. 5.6 depicts the variation of the transmission ratio of the CVT in which is possible to appreciate the step-less variation of the transmission ratio.

5.3   Contribution

The results shown in this chapter have been published in [32].

CHAPTER 6

Conclusions

In this doctoral thesis a new topology for the Diesel Engine Common Rail System has been proposed. The novel idea shown in this work is the introduction of a *Continuously Variable Transmission* (CVT) between the internal combustion engine and the high pressure pump. Firstly a literature review of the state of the art of the common rail pressure regulation is analysed and discussed. Then the model of a two stage planetary traction drive is developed and is used to compute the efficiency of the transmission. The model is derived considering the Visco-Elastic coupling between the component of the transmission and is suitable simulate the efficiency of transmission in the operating point of interest. Moreover, the model can be used to optimize the geometry of the transmission in order to maximize the efficiency and minimize the size.

A new control strategy for the high pressure regulation with a CVT is proposed. This new method consists in two control loops that drive the *Fuel Metering Unit* (FMU) and the CVT decoupling these two actuators. The FMU is controlled using an *Model Reference Adaptive Controller* (MRAC) that take into account the high pressure pump speed. In this way, the control loop adapts is actuation on the basis also of the second controller. The CVT is controlled using a Fuzzy approach that, according the defined rules, is able to adjust the common rail pressure minimizing the high pressure pump speed.

The new proposed topology has been tested on a proof of concept. The experiment is performed on a presupply pump test bench with a scaled version of the Common Rail System. This choice is due to technical difficulties in the realization of a complete test bench. Nevertheless, this experiment gives a clear idea about the effectiveness of the

concept and shows encouraging results for future development.

Considering the results obtained in this years, the next step is the creation of a complete test bench with a real high pressure pump and a suitable transmission to validate the proposed approach.

References

[1] P. A. Lakshminarayanan and A. Agarwal, *Design and Development of Heavy Duty Diesel Engines: A Handbook.* Springer, 2020.

[2] M. Rundo, "Models for flow rate simulation in gear pumps: A review," *Energies*, vol. 10, no. 9, p. 1261, 2017.

[3] A. Balluchi, A. Bicchi, E. Mazzi, A. S. Vincentelli, and G. Serra, "Hybrid modelling and control of the common rail injection system," *International Journal of Control*, vol. 80, no. 11, pp. 1780–1795, 2007.

[4] A. Balluchi, A. Bicchi, E. Mazzi, A. L. Sangiovanni-Vincentelli, and G. Serra, "Hybrid multi-rate control of the common-rail," in *Proceedings of 2007 European Control Conference (ECC)*, pp. 54–61, IEEE, 2007.

[5] P. Lino, B. Maione, and A. Rizzo, "Nonlinear modelling and control of a common rail injection system for diesel engines," *Applied Mathematical Modelling*, vol. 31, pp. 1770–1784, 2007.

[6] P. Lino, B. Maione, and A. Rizzo, "Multi-domain modelling and control in mechatronics: the case of common rail injection systems," *Robotics, Automation and Control*, pp. 494–517, 2008.

[7] C. Gauthier, O. Sename, L. Dugard, and G. Meissonnier, "An H∞ linear parameter-varying (LPV) controller for a diesel engine common rail injection system," in *Proceedings of 2007 European Control Conference (ECC)*, pp. 1932–1939, 2007.

[8] C. Gauthier, O. Sename, L. Dugard, and G. Meissonnier, "An LFT approach to H∞ control design for diesel engine common rail injection system," *Oil &*

Gas Science and Technology - Revue d'IFP Energies nouvelles, vol. 62, no. 4, pp. 513–522, 2007.

[9] C. Gauthier, O. Sename, L. Dugard, and G. Meissonnier, "Modelling of a diesel engine common rail injection system," *IFAC Proceedings Volumes*, vol. 38, no. 1, pp. 188–193, 2005.

[10] C. Gauthier, O. Sename, L. Dugard, and G. Meissonnier, "Some experimental results of an H∞ -LPV controller applied to a diesel engine common rail injection system," *IFAC Proceedings Volumes*, vol. 40, no. 10, pp. 417–424, 2007.

[11] C. Gauthier, *Commande multivariable de la pression d'injection dans un moteur diesel common rail.* Theses, Institut National Polytechnique de Grenoble - INPG, May 2008.

[12] W. Chatlatanagulchai, T. Aroonsrisopon, and K. Wannatong, "Robust common-rail pressure control for a diesel-dual-fuel engine using QFT-based controller," tech. rep., SAE Technical Paper, 2009.

[13] S. Hong, J. Shin, and M. Sunwoo, "Common rail pressure controller for diesel engines using an empirical model," in *Proceedings of 2012 IEEE Vehicle Power and Propulsion Conference*, pp. 887–892, IEEE, 2012.

[14] S. Hong, J. Shin, J. Sohn, I. Park, and M. Sunwoo, "Coordinated control strategy for the common-rail pressure using a metering unit and a pressure control valve in diesel engines," *Proceedings of the Institution of Mechanical Engineers, Part D: Journal of Automobile Engineering*, vol. 229, no. 7, pp. 898–911, 2015.

[15] S. Hong, J. Shin, I. Park, M. Sunwoo, J. Jeon, and C. Choi, "Robust common rail pressure control algorithm for light-duty diesel engines," *IFAC Proceedings Volumes*, vol. 46, no. 21, pp. 717 – 722, 2013.

[16] M. Rivas, O. Sename, E. Witrant, C. Caillol, and P. Higelin, "Common rail injection system controller design using input-to-state linearization and optimal control strategy with integral action," in *Proceedings of 2013 European Control Conference (ECC)*, pp. 1994–1999, IEEE, 2013.

[17] H. Wang, D. Zheng, and Y. Tian, "High pressure common rail injection system modeling and control," *ISA Transactions*, vol. 63, pp. 265 – 273, 2016.

[18] G. Carbone, L. Mangialardi, and G. Mantriota, "Fuel consumption of a mid class vehicle with infinitely variable transmission," *SAE International Journal of Engines*, vol. 110, pp. 2474–2483, 2001.

[19] F. Bottiglione, S. De Pinto, G. Mantriota, and A. Sorniotti, "Energy consumption of a battery electric vehicle with infinitely variable transmission," *Energies*, vol. 7, pp. 8317–8337, 2014.

[20] G. Carbone, L. Mangialardi, B. Bonsen, C. Tursi, and P. Veenhuizen, "CVT dynamics: Theory and experiments," *Mechanism and Machine Theory*, vol. 42, no. 4, pp. 409 – 428, 2007.

[21] F. Verbelen, S. Derammelaere, P. Sergeant, and K. Stockman, "A comparison of the full and half toroidal continuously variable transmissions in terms of dynamics of ratio variation and efficiency," *Mechanism and Machine Theory*, vol. 121, pp. 299 – 316, 2018.

[22] S. H. Loewenthal, "Spin analysis of concentrated traction contacts.," *Journal of mechanisms, transmissions, and automation in design*, vol. 108, no. 1, pp. 77–85, 1986.

[23] S. Maldotti, *Sulla energia dissipata in alcuni organi di macchina.* PhD thesis, Alma Mater Studiorum, 2009.

[24] L. De Novellis, G. Carbone, and L. Mangialardi, "Traction and efficiency performance of the double roller full-toroidal variator: A comparison with half- and full-toroidal drives," *Journal of Mechanical Design, Transactions Of the ASME*, vol. 134, no. 7, 2012.

[25] B. J. Hamrock, *Fundamentals of Fluid Film Lubrication (The McGraw-Hill series in mechanical engineering).* McGraw-Hill, 1994.

[26] G. Carbone, L. Mangialardi, and G. Mantriota, "A comparison of the performances of full and half toroidal traction drives," *Mechanism and machine theory*, vol. 39, no. 9, pp. 921–942, 2004.

[27] M. Tomaselli, P. Lino, and G. Carbone, "Modelling and efficiency formulation of a planetary traction drive CVT," in *Proceedings of 9th IFAC Symposium on Advances in Automotive Control AAC 2019*, pp. 411 – 416, 2019.

[28] M. Tomaselli, F. Bottiglione, P. Lino, and G. Carbone, "Nuvinci drive: Modeling and performance analysis," *Mechanism and Machine Theory*, vol. 150, p. 103877, 2020.

[29] K. Prinz, W. Kemmetmüller, and A. Kugi, "Mathematical modelling of a diesel common-rail system," *Mathematical and Computer Modelling of Dynamical Systems*, vol. 21, no. 4, pp. 311–335, 2015.

[30] M. Tomaselli, P. Lino, G. Carbone, and M. Roncone, "Common-rail pressure control using a model reference adaptive control approach," in *Proceedings of 2019 IEEE International Conference on Systems, Man and Cybernetics (SMC)*, pp. 1907–1912, IEEE, 2019.

[31] M. Tomaselli, P. Lino, G. Carbone, and M. Roncone, "Common-rail pressure control using a continuously variable transmission (CVT)," in *Proceedings of 2020 7th International Conference on Control, Decision and Information Technologies (CoDIT)*, vol. 1, pp. 1035–1039, IEEE, 2020.

[32] M. Tomaselli, P. Lino, G. Carbone, and M. Roncone, "Proof of concept validation of a common-rail pressure control using a continuously variable transmission (CVT)," in *Proceedings of 2020 7th International Conference on Control, Decision and Information Technologies (CoDIT)*, vol. 1, pp. 1024–1028, IEEE, 2020.